

***ADHESION AND OPTOELECTRONIC PROPERTIES OF  
ORGANIC LIGHT EMITTING DEVICES (OLEDs) AND  
HYBRID ORGANIC-INORGANIC LIGHT EMITTING  
DEVICES (HOILEDs) WITH TiO<sub>2</sub> NANO-PARTICLES***

**MOMODU, Damilola Yusuf**

**A THESIS SUBMITTED TO THE FACULTY OF  
AFRICAN UNIVERSITY OF SCIENCE AND TECHNOLOGY  
IN CANDIDACY FOR A MASTERS DEGREE**

**RECOMMENDED FOR ACCEPTANCE BY DEPARTMENT OF  
MATERIAL SCIENCE AND ENGINEERING**

**ADVISER: WINSTON O. SOBOYEJO**

**DECEMBER 2010**

**THE VOCATION, IS TO MAKE MY RESEARCH  
A PASSION FOR ME AND GENERATIONS YET  
UNBORN, FOR IT IS THE ONLY TRUE SPICE OF LIFE...**

**Momodu, Y. Damilola**

**© Copyright by Momodu Damilola Yusuf**

**All rights reserved**

**(2010)**

**With love,**  
**this thesis is dedicated to my parents,**  
**Mr. A.B Momodu and Late Mrs. Cecilia Momodu**  
**for the gift of greatness they have given me.**

## ABSTRACT

This study examines the basic operation of an Organic Light Emitting Device (OLED) and Hybrid Organic-Inorganic Light Emitting Devices (HOILED) by looking at the individual characteristics of the each layer which makes up the entire device. Adhesion analysis and different types of layer characterization were carried out. First of all, the material of interest was deposited on AFM tips, clean 1 sq. inch glass substrates and ITO-coated glass with subsequent final fabrication of the device. Characterization was carried out to determine the Surface, Electrical and Optical properties. Results obtained showed improvements in all layer properties when annealed. Deposition techniques and parameters used also affected the final device properties.

Atomic Force Microscopy (AFM) measurements of adhesion between interacting layers were carried out for both normal and hybrid layers on glass and ITO. Results obtained were quantified in terms of average pull-off forces and corresponding adhesion energies were gotten by incorporating forces into theoretical models. This forms a path to further establishing devices with suitable design structures and materials combinations.

## TABLE OF CONTENTS

	<b>PAGE</b>
ACKNOWLEDGEMENT .....	iii
ABSTRACT .....	v
TABLE OF CONTENTS .....	vi
LIST OF TABLES .....	ix
LIST OF FIGURES .....	x
CHAPTER ONE .....	13
1.0 Introduction .....	13
1.1 Background .....	13
1.2 Scope of Work .....	15
1.3 Summary and Layout of Thesis .....	15
CHAPTER TWO .....	16
2.0 Background Theory and Literature Review .....	16
1.4 2.1 Organic Light Emitting devices (OLEDs).....	16
2.1.1 Introduction .....	16
2.1.2 Physical Structure of OLED and Theory of Operation.....	16
2.1.3 Trends of OLED Development in the Future and its Applications.....	20
2.2 Hybrid Organic-Inorganic Device (HOILED).....	22
2.3 Theory of Thin-film Deposition and Processing Techniques .....	23
2.3.1 Introduction .....	23
2.3.2 Anode Deposition by R.F Magnetron Sputtering and Annealing Methods .....	23
2.3.2.1 Annealing Methods.....	25
2.3.3 Spin Coating of Organic Layers .....	25
2.3.4 Thermal Evaporation of Cathode Layer.....	27
2.4 Adhesion Theory.....	28

2.4.1	Adhesive Contact Models .....	29
2.5	Charge Transport in OLEDs and HOILEDs.....	37
2.5.1	Introduction .....	37
2.5.2.	Fowler-Nordheim tunneling .....	37
2.5.3.	Schottky Barrier.....	39
2.6	Earlier research work and contributions to present OLED technology .....	40
CHAPTER THREE.....		45
3.	Characterization and Adhesion Analysis in OLEDs and HOILEDs .....	45
3.1	Experimental Methods .....	45
3.1.1	Materials.....	45
3.1.2	Deposition of ITO Thin-Film layer on glass Substrate and AFM tips.....	46
3.1.2.1	Cleaning of glass slides.....	46
3.1.2.2	Preparation of AFM tips.....	47
3.1.2.3	Deposition of Indium Tin-Oxide by Sputtering.....	47
3.1.2.4	Annealing of ITO Thin-Film layer and AFM tips .....	48
3.1.3	Deposition of PEDOT:PSS Thin-Film layer on glass substrate and ITO- coated glass	48
3.1.4	Deposition of MEH-PPV Thin-film layer on Glass and ITO-coated glass.....	49
3.1.4.2	Spin Coating of MEH-PPV on glass and ITO-coated glass.....	50
3.1.5	Deposition of Aluminum thin-film on glass substrates .....	51
3.1.6	Deposition of MEH-PPV+TiO <sub>2</sub> hybrid layer .....	51
3.1.7	Fabrication of Organic Light Emitting Device.....	52
3.1.8	Fabrication of Hybrid OLEDs.....	52
3.2	Thin-Film Layer and Device Characterization.....	52
3.2.1	Surface Morphological Characterization .....	53
3.2.2	Optical Characterization.....	54

3.2.3	Adhesion Measurements with Atomic Force Microscopy .....	54
3.2.4	Electrical Characterization of Layered Structures and Device.....	56
3.3	Results and Discussions .....	58
3.3.1	Surface Morphological Characterization of Thin-Film Layers .....	58
3.3.2	Electrical Characterization and Optical Analysis of Thin-Film Layers .....	66
3.3.3.	Optical Characterization of Thin-Film layers.....	69
3.3.4	I-V Characterization and Spectral Analysis of light emitted from device .....	74
3.3.5	Spectral Analysis of light emitted from device .....	79
3.3.5.1	Device Spectral Analysis .....	79
3.3.6	Adhesion Measurements .....	81
3.3.7	Implications .....	84
CHAPTER FOUR.....		86
4.0	Summary and Suggestions for Future Work.....	86
5.0	References .....	88

## LIST OF TABLES

<b>Table</b>	<b>PAGE</b>
3.0 Spin Coating Recipe.....	50
3.1 Roughness average and thickness for different layered structures.....	58
3.2 Sheet resistance values at different point for unannealed ITO layer.....	67
3.3 Sheet resistance values at different points for annealed ITO on glass layer.....	67
3.4 Sheet resistance values at different points for annealed ITO on glass layer.....	68
3.5 Sheet resistance values at different points on a PEDOT:PSS layer.....	68
3.6 Sheet resistance values at different points on a PEDOT:PSS layer.....	68
3.7 Sheet resistance values at different points for a layer of PEDOT:PSS on ITO.....	69
3.8 Sheet resistance values at different points for Aluminium on glass.....	69
3.9 Average adhesion force data for various pairwise interactions of OLED and HOILED layers.....	83
3.10 Average adhesion energies for various pairwise interactions of OLED and HOILED layers.....	84

## LIST OF FIGURES

<b>Figure</b>	<b>PAGE</b>
2.0 Structure of an OLED.....	17
2.1 Description of the Hole and Electron Injection mechanism.....	18
2.2(a) MEH-PPV structure.....	19
2.2(b) PEDOT:PSS structure.....	19
2.3 OLED Display Revenue Forecast.....	21
2.4 R.F. Magnetron Sputtering System.....	24
2.5 Spin Coating device set-up.....	26
2.6(a) Schematic of Thermal Evaporation.....	27
2.6(b) Thermal Evaporator.....	28
2.7 Lennard – Jones and Dugdale Surface force laws.....	35
2.8 Diagram to illustrate charge tunneling with energy level scheme.....	38
3.1 MEH-PPV in 25 ml beaker during stirring beaker during stirring at 695 rpm.....	49
3.2 MEH-PPV after filtration and ready for spin coating.....	49
3.3 Carbolite Oven used for annealing and drying samples.....	51
3.4 Schematic for Optical Characterization.....	53
3.5 Schematic force-displacement curve depicting the various stages of cantilever-surface engagement.....	55
3.6 Keithley set-up for Electrical Characterization.....	57
3.7 Surface Profile for ITO on glass showing ITO thickness.....	59
3.8 Surface Profile for ITO and glass showing roughness.....	59
3.9 Surface Profile for PEDOT on glass showing roughness.....	60
3.10 Surface Profile PEDOT on ITO showing thickness.....	60

<b>Figure</b>	<b>PAGE</b>
3.11 Surface Profile for PEDOT on ITO showing roughness.....	61
3.12 Surface Profile for MEH-PPV on glass showing thickness.....	61
3.13 Surface Profile for MEH-PPV on glass showing roughness.....	62
3.14 Surface Profile for Aluminum on glass showing roughness.....	62
3.15 Surface Profile for Aluminum on glass showing thickness.....	63
3.16 Surface Profile for PEDOT on ITO showing thickness (heated at 250 °C).....	63
3.17 Surface Profile for PEDOT on ITO showing roughness (heated at 250 °C).....	64
3.18 SEM image for ITO showing surface morphology.....	64
3.19 SEM image for PEDOT:PSS showing surface morphology.....	65
3.20 SEM image for MEH-PPV showing surface morphology.....	65
3.21 SEM image for MEH-PPV on ITO showing surface morphology.....	66
3.22 Transmittance Spectra of a plane glass.....	71
3.23 Transmittance Spectra of ITO on glass substrate (unannealed).....	71
3.24 Transmittance Spectra of ITO on glass substrate (annealed).....	72
3.25 Transmittance Spectra of PEDOT:PSS on glass substrate.....	72
3.26 Transmittance Spectra of PEDOT:PSS on ITO.....	73
3.27 Transmittance Spectra of MEH-PPV on glass.....	73
3.28 Transmittance Spectra of MEH-PPV + TiO <sub>2</sub> on glass.....	74
3.29 I-V Characteristic curve for a HOILED with forward bias current.....	75
3.30 I-V Characteristic curve for an OLED with forward bias current.....	76
3.31 J-V Characteristic curve for an OLED with forward bias current.....	76
3.32 J-V Characteristic curve for an OLED with forward bias current.....	77
3.33 I-V Characteristic curve for an OLED with excess forward bias.....	77

<b>Figure</b>	<b>PAGE</b>
3.34 I-V Characteristic curve for an OLED with forward bias current after 10 mins.....	78
3.35 I-V Characteristic curve for an OLED with forward bias current after 25 mins.....	78
3.36 I-V Characteristic curve for an OLED with forward bias current after 45 mins.....	79
3.37 Spectrum of light emitted (from high magnification showing noise on background).....	80
3.38 Spectrum of light emitted (from high magnification showing noise on background).....	80
3.39 Spectrum of light emitted (from high magnification with noise unfiltered).....	81
3.40 Average adhesion forces obtained for OLED/HOILED layer structures.....	82
3.41 Average adhesion energies obtained for OLED/HOILED layer structures.....	83

## CHAPTER ONE

### 1.0 Introduction

#### 1.1 Background

Since their original development by Friend et al.<sup>[27]</sup> about twenty years ago, organic light emitting devices (OLEDs) have received considerable attention due to their potential for low cost applications in “soft” lighting and displays.<sup>[1-5]</sup> Furthermore, the potential to pattern and stamp them into micron- and nano-scale patterns has made them potential candidates to replace liquid crystal displays that are based on inorganic silicon-based light emitting devices. However light emitting devices are limited by their relatively low lifetimes due to the limited stability in the presence of oxygen and water vapor.<sup>[34]</sup> They also have limited quantum efficiencies and undergo a range of degradation mechanisms during exposure to light and water vapor/oxygen in the environment.

Along with the general advancement and optimization of organic light emitting devices, demand for solutions to the limitations of this technology is fueling an in depth research. These include detailed adjustment and optimization of various electrical, spectral properties, design of device structure layout, charge transport techniques etc. to boost efficiency and lifetime of these devices.

Most recently, inorganic materials have been doped into the layers within OLEDs in an effort to promote charge and light transport.<sup>[64]</sup> Such doping has also been suggested as a way of improving charge transport in hybrid organic-inorganic light emitting devices in which charge recombination can occur before electron/hole pairs reach the electrodes.

Other contributions from scientists include an attempt to balance the charge carriers in organic light emitting devices by incorporating a blend of PBD layer in between the organic NPB layer and Alq<sub>3</sub> electron transmission layer (ETL). This produced a device with enhanced life span and luminance efficiency.<sup>[7]</sup>

Other scientists have introduced wide band gaps impurities in form of doping the electron transport layer (ETL) or hole buffer layer (HBL) with polymer materials to increase the device operating current, lifetime and luminance efficiency.<sup>[8]</sup>

Although extensive research is ongoing in this field, overall device power efficiencies are still considerably low. However some improved efficiencies are being reported even though there are no details about the structure yet, the future of OLED technology remains promising.<sup>[9]</sup>

In all the numerous approaches reported on research into this device, very little attention is being reported on doping organic layers with varying compositions of metallic oxide nanoparticles or actually analyzing the optoelectronic and adhesive properties of these layers being deposited for the OLEDs and HOLEDs. The adhesive energies of these individual layers affects charge transport through partial debonding between layers. Relatively high current densities in areas of partial contact could lead to localized heating and oxidation phenomena which affects general OLED performance.<sup>[46]</sup> Thus, there is the need to obtain materials with good adhesion energies to aid high surface contact.

## **1.2 Scope of Work**

This study presents the results of an experimental study of the optoelectronic properties of simple model OLED and HOILED systems. Surface, optical and electrical properties are characterized in each of these layers and the potential effects of adding inorganic TiO<sub>2</sub>-nano particles in MEH-PPV active layer of HOILEDs. Furthermore, the underlying effects of adhesion are examined along with the potential degradation mechanisms that occur during exposure to laboratory air.

## **1.3 Summary and Layout of Thesis**

The results of an initial study of the electrical properties of model OLED and HOILED structures are presented in this thesis. Following the introduction, a review of the relevant literature is presented in **Chapter Two (2)**. The fabrication and characterization of the model layered structures and complete devices are then described in **Chapter Three (3)** which include initial measurements of the layer thickness and device performance characteristics.

Conclusion and suggestions for future work are presented in **Chapter Four (4)**.

The thesis contains 80 pages, 52 figures, 11 tables, 32 equations and 85 references.

## CHAPTER TWO

### 2.0 Background Theory and Literature Review

#### 1.4 2.1 Organic Light Emitting devices (OLEDs)

##### 2.1.1 Introduction

An Organic Light Emitting Device/Diode (OLED) is simply a thin-layered device in which there exists an emissive electroluminescent layer made from organic compounds that responds to electric current. The conversion of electrical energy into light requires the generation of electrons and holes within the device, and the possible recombination of these charges to produce an “exciton” (a bound state of electron and hole).

A driving force has to be present in form of an electrostatic force to move these charges from the positive and negative electrode to the recombination site. Holes generally move faster than electrons in organic materials and as such, places the recombination site closer to the emissive layer at the cathode <sup>[11]</sup>.

##### 2.1.2 Physical Structure of OLED and Theory of Operation

A typical OLED is a thin-layered device composed of two electrodes (transparent anode and metallic cathode) which sandwiches an electroluminescent organic layer on a glass bottom plate (substrate) and top plate (Seal).

The organic layer comprises of a hole injection layer (HIL), a hole transport layer (HTL), an emissive layer (EML) and an electron transport layer (ETL). When an electric voltage is applied, the injected positive and negative charges combine in the emissive layer to give light.<sup>[14]</sup> The organic molecules of this layer are normally electrically conductive as a result of de-localization of pi-electrons caused by conjugation over parts of the molecule or the entire molecule. They are sometimes referred to as organic semiconductors due to their range of conductivity values. The conduction bands and valence bands in inorganic semiconductors correspond respectively to the Lowest Unoccupied Molecular Orbital

(LUMO) and Highest Occupied Molecular Orbital (HOMO) in organic devices <sup>[11]</sup>.

The main distinguishing factor that differentiates the OLED from much common inorganic light emitting devices is the organic layer ( e.g. MEH-PPV) on a transparent glass substrate, rather than the semiconductor Si-wafers.

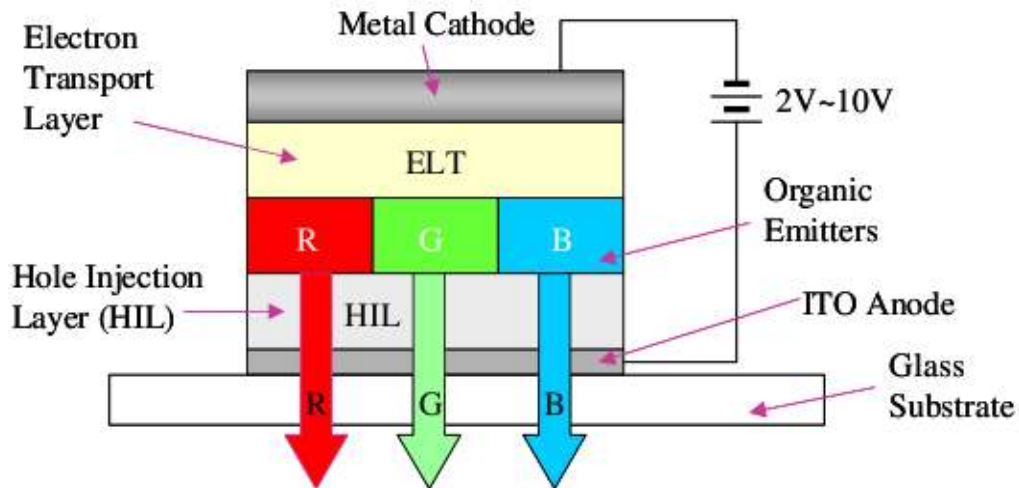


**Fig. 2.0: Structure of OLED**<sup>[12]</sup>

Most basic organic light emitting devices consist of bi-layered structure that includes a conductive and an emissive layer. The reason for this multi-layered fabrication is to improve device efficiency by creating an aid to charge injection or blockage at the electrodes thereby balancing the amount of change carriers in the device. <sup>[7][15][16]</sup>

## **Theory of Operation**

The operation of an organic light emitting device involves the application of a bias voltage across the anode and the cathode.

Charge transport occurs through the device between the anode and cathode, thus producing electroluminescent light from the organic layer. As electrons are injected into the LUMO of the organic layer during electron current flow, they are also withdrawn from the HOMO of the organic layer. They form an “exciton” in the emissive layer and further decay of this excited state to a lower energy level results in a relaxation of the energy levels of the electron, accompanied by the emission of distinct radiation with a frequency in the visible region. <sup>[11]</sup> The frequency of the radiation depends on the band gap of the material, in this case, the energy difference between the HOMO and LUMO.

The anode material is designed to be transparent. This is done to enable the emitted radiation from the organic layer to be visible when the device is connected to a voltage source.

The most widely used material for the anode material is Indium Tin-Oxide (ITO), because of its transparency. ITO also has a high work function that promotes hole injection into the HOMO level of the organic layer. <sup>[17]</sup>

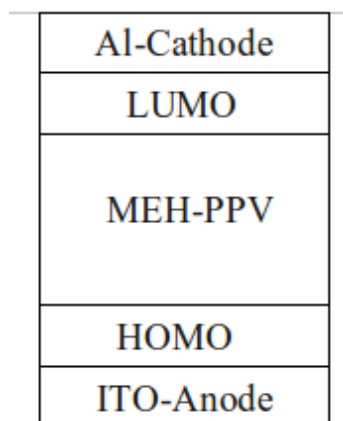


**Fig 2.1: Description of the Hole and Electron Injection Mechanism**

A common example of organic layer is the organic polymer called poly(2-methoxy-5-(2'-ethylhexyloxy)-1,4-phenylene vinylene) (MEH-PPV) or poly(3,4-ethylenedioxythiophene) polystyrene sulfonate (PEDOT:PSS). MEH-PPV is a conjugated conductive polymer (Fig. 2.2(a)) that is soluble in organic solvents such as chloroform or tetrahydrofuran (THF). Their main advantage over non-polymeric organic semiconductors is the possibility of processing the polymer to form useful and robust structures.<sup>[27]</sup> The choice of polymer is due to its favourable HOMO level which falls between the work function of the ITO anode and reduces the barrier for hole injection into the HOMO level of the organic layer from the ITO layer where holes are created.<sup>[11]</sup>

This can be seen from **Fig 2.1** where the layered structure indicates the HOMO and LUMO of the organic layer with respect to the ITO anode layer. The closer the energy level between the site of creation of the holes and the HOMO of organic layer, provides an easy injection of holes from the anode to the HOMO level of organic layer.

On the other hand, the cathode material has to possess a low work function which promotes the easy injection of electrons into the LUMO of the organic layer. A low work function means that electrons are easily lost from the surface of the electrode and are injected into the LUMO of the organic layer. Examples of suitable cathodes include Aluminium (Al), Barium (Ba) and Calcium (Ca). Aluminium is preferred in most OLEDs because it is less reactive compared to others (Ca and Ba) in degradation ability.

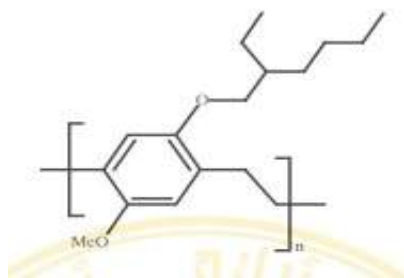
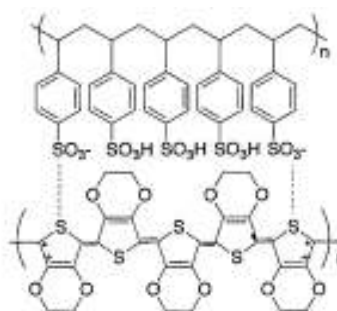


**Fig 2.2: a) MEH-PPV structure**



**b) PEDOT:PSS structure**

PEDOT:PSS is also used as a hole injection layer and smoothing layer in some devices.<sup>[10]</sup> This serves two purposes with its structure shown in Fig. 2.2 (b). PEDOT:PSS is one of the most important conducting polymers synthesized in organic electronics field. The combination of relatively high conductivity with optical transparency makes it suitable for numerous applications including OLEDs.<sup>[12]</sup>

### 2.1.3 Trends of OLED Development in the Future and its Applications

Organic light emitting devices are considered to be the “screens” and “light” of the future.<sup>[18]</sup> Unlike liquid crystal displays (LCDs) and plasma displays, which require thin-film processing on two glass plates, OLEDs can be fabricated on one sheet of glass or plastic. This greatly simplifies the manufacturing process. It also makes OLEDs thinner than competing display technologies.

In addition, the charge combination process causes very little time delay resulting in its fast response time. The large viewing angles ( $\sim 160^\circ$ ) in all directions also make OLEDs candidates for use of color filters. This reduces their power consumption, with improved transmission efficiency.

However with all desirable device properties listed above, the lifetime of OLEDs is still a major cause for concern. Also the brightness of OLED display pixels reduces with working time. This has been attributed to interaction with environmental species (mostly oxygen and water vapor) and the occurrence of blisters, carbonization<sup>[35]</sup> and spiral buckles.<sup>[36]</sup> Such failure modes have stimulated a global effort to improve the overall efficiencies and lifetimes of OLEDs.

Promising applications which offer unique advantages of high contrast, low cost, wide viewing angles, light weight designs and ease of application all in one device make certain

industry experts claim that OLEDs will take over the lighting and display market. However, others are not as enthusiastic and claim the technology is too advanced to be squeezed in a one-size-fits-all approach. <sup>[1]-[6][18][19]</sup>

According to reports by Display Search forecasts in 2009, the total OLED revenue is expected to grow in the next six years (Fig. 2.3).<sup>[18]</sup> However there is a need to address the issues of sensitivity to environment and charge transport.

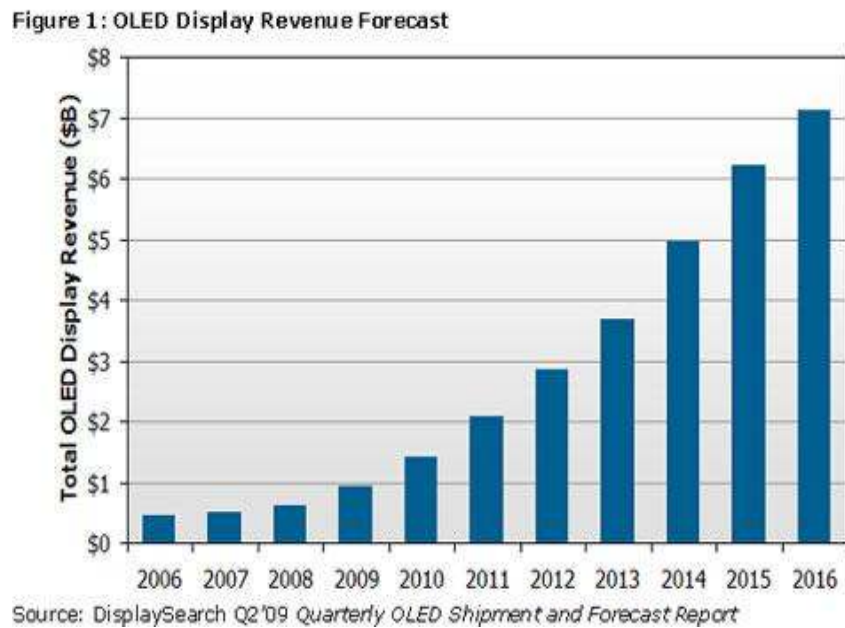


**Fig. 2.3: OLED Display Revenue Forecast**<sup>[18]</sup>

## 2.2 Hybrid Organic-Inorganic Device (HOILED)

The emergence of Organic light emitting devices (OLEDs) as the next generation lighting and electronic display technologies has created an urgent need to solve the problem of instability in air. This led to experimenting a possible solution by introducing a stable charge injection site or an encapsulation-free hybrid organic-inorganic LED with a simple structure that is nonreactive to the atmosphere. <sup>[45]</sup>

The incorporation of metallic oxides (mainly transition metals with different unique characteristics into the layout of OLED structure has led to the invention of hybrid organic-inorganic light emitting devices (HOILEDs).

Much interest has been directed towards studying the nature of hybrid organic-inorganic nano-structures, owing to their possibility of combining the electrical properties of semi-conducting organic polymers with the special optical properties of inorganic nanostructures like rods, particles and thin films. <sup>[48-63]</sup> Examples of these unique characteristics include high transparency, good conductivity, tune-able and large variety of possible nano-structures.

Hybrid organic/inorganic light emitting devices have an architecture that makes use of metallic oxides (such as TiO<sub>2</sub>, MoO<sub>3</sub>, ZnO etc.) as charge-injecting materials into light emitting polymers. Also, using a cathode material that is not reactive gives them stability in air, compared to that of normal OLEDs.

The resulting electroluminescent devices exhibit higher brightness levels at low voltages. They also operate more suitably in air. Prior researchers have demonstrated the enhanced operation of HOILED. These include their increased efficiency (through the chemical interactions between the metallic oxides and organic layer and their carrier injection characteristics. <sup>[21][22][23][24]</sup>

Konekap et al.<sup>[25]</sup> have produced an electroluminescent device in which ZnO was used as a near UV-emitter in combination with PEDOT: PSS as hole-injection material. However ZnO has not been used as cathode in OLEDs. This study will extend the prior work to a HOILED system with TiO<sub>2</sub>-nano particles and MEH-PPV in the active layer.

## **2.3 Theory of Thin-film Deposition and Processing Techniques**

### **2.3.1 Introduction**

Thin film is the term used to describe a technique for depositing passive circuit elements on an insulating substrate for e.g. glass with coating thickness between the nano-meter or micrometer scales. The techniques that are used for thin-film deposition include; R.F Magnetron Sputtering, Spin Coating and Thermal Evaporation. These will be discussed in detail in this section.

### **2.3.2. Anode Deposition by R.F Magnetron Sputtering and Annealing Methods**

This section will describe the R.F sputtering technique for depositing the anode material on a clean glass substrate. The set-up used for R.F sputtering is shown in **Fig. 2.4**

Sputtering is one of the most widely used technique for deposition of the anode layer of organic electronic devices. This method presents a higher purity and better controlled composition which provides film with greater adhesive strength and homogeneity. Indium Tin Oxide (ITO) is the anode material generally used for fabrication of Organic Light Emitting Devices and their Hybrid Organic-Inorganic Light Emitting Devices. This is due to its high transparency, conducting capacity and high adhesive property.<sup>[65]</sup> The sputtering system can be powered by different modes which include:

- (i) R.F. Magnetron sputtering mode
- (ii) Electron beam sputtering mode
- (iii) DC sputtering mode

Our focus is mainly on the R.F sputtering mode because this mode of operation was used in fabrication of our devices for depositing ITO on glass.

The R.F sputtering process involves the creation of a gas plasma at very low pressure, using an inert gas and applying a high R.F frequency power via a frequency generator across the anode and cathode of the sputtering chamber. The cathode is used as the source/target holder, while the anode is used as a substrate holder.



**Fig. 2.4: R.F Magnetron Sputtering set-up**

By momentum transfer, the source material of Indium Tin-Oxide (ITO) subjected to intense bombardment by  $\text{Ar}^+$  ions, ejects ITO ions from its surface. The injected ITO ions are deposited as pure thin -films onto the substrate. The advantage of the R.F Magnetron Sputtering is its less restrictive use for cases requiring high deposition rates and low substrate temperatures in both conducting and non-conducting targets.

The basic sputtering process however remains the same irrespective of the sputtering system

used. Transparent and conducting ITO films are thus deposited with an increase in sputter power increasing the rates of deposition of ITO layers on the substrate.

### **2.3.2.1 Annealing Methods**

The annealing process is the heating up of the ITO thin-film layers to a particular temperature beyond which the structure changes from an amorphous state to a crystalline state. The annealing process carried out after the sputtering process changes the electrical properties of the layer. <sup>[65][66]</sup> For example, the sheet resistance is reduced by a factor of two when annealed at 250<sup>0</sup>C for an hour. This enhances conductivity if the ITO transparent layer. Other characteristics, such as uniformity of the layer with annealing are improved to some extent. Although, general changes are also dependent on annealing time and temperature. <sup>[67][68]</sup>

### **2.3.3 Spin Coating of Organic Layers**

Spin Coating is a common method used for application of organic layers on flat substrates of moderate dimensions in OLEDs. The theory of spin coating is based the centripetal acceleration force applied to a fluid which is deposited on the glass surface. The set-up for Spin Coating process is shown in **Fig. 2.5**

The spin coating process involves three basic stages:

Dispense mode or step for evenly distributing the organic layer. It can be operated on a static or dynamic platform depending on the properties of the fluid and desired thickness.

High spin mode or step for thinning out the fluid to a desired film thickness. This usually involves ultra-high speeds of the order of thousands of rotations per minute (rpm)

Final mode or step which is a drying step to remove excess fluid from the surface of the substrate. This step can also be omitted and the sample can be dried in an oven at

moderate temperature.



**Fig. 2.5: Spin Coating device set-up**

Generally factors affecting the final properties of the organic material spin coated include:

Spin speed

Acceleration

Spin time

Exhaust etc.

Spin speeds greatly determine the final thickness of material deposited and velocity of the enveloped air over the spinning substrate affects film thickness to an extent. The operation modes and spin parameters are all incorporated into a program recipe which accompanies a spin coating process. The program recipe number containing how spin coating will be done are all displayed on the user interface screen of the spin coating machine.

### 2.3.4 Thermal Evaporation of Cathode Layer

Thermal Evaporation is a deposition technique that is used for coating many types of materials (organic and inorganic) in a highly evacuated chamber. The scope of this work will focus mainly on the thermal evaporation of inorganic materials, such as metallic cathode layers of the OLEDs and HOILEDs.

The material to be deposited is normally heated to its vaporized state by a high voltage applied as heat energy to a heating filament. The filament heats up the metal, which is then irradiated in straight lines at very high vacuum, onto the substrate placed directly above it. The heating filament or coil is usually of higher melting temperature and a chart of different combination of filaments with their respective cathode elements is used for selection.

The Thermal Vacuum Evaporation technique is most suitable for deposition of highly-reactive cathode materials such as aluminum and calcium. These are materials that are difficult to work with under normal atmospheric conditions. The method is clean and allows a better contact between the layer of deposited material and the surface upon which it has been deposited. Since evaporation beams travel in straight lines at very high vacuum, precise and uniform patterns are produced. A schematic of thermal evaporation in vacuum is shown in **Fig. 2.6**.

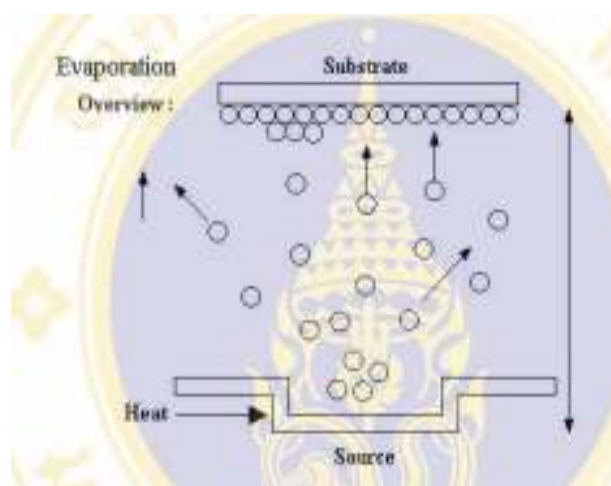


**Fig. 2.6(a): Schematic of Thermal Evaporation<sup>[69]</sup>**



**Fig. 2.6 (b): Thermal evaporator**

Other methods of deposition of such metals include the plasma enhanced chemical vapour deposition (PEVD) where chemicals are reacted in a plasma chamber in vapour phase and are deposited either upwards or downwards onto the substrate.

## **2.4 Adhesion Theory**

As scale length decreases, adhesive forces become increasingly important. These adhesive forces contribute to the charge transport across layers of organic light emitting devices.<sup>[70]</sup>

Degradation by de-lamination between layers during charge transport creates a need for detailed understanding of the adhesive studies between layers of organic light emitting devices and HOILEDs.<sup>[46]</sup>

**Adhesion** is any attraction process between dissimilar molecular species that can potentially

bring them in direct contact. The most common forces existing between adhesive contacts are the Van der Waal forces. However contact may also be induced by hydrogen bonds or primary bonds.

**Surface energy** can be described as the work required to build a unit area of a particular surface. Several models have been developed to model the adhesion and contact between different types of materials and contact geometries. From a fracture mechanics perspective, the adhesion energy  $\gamma$  corresponds to the mode I fracture energy  $G$ . For crack growth between two dissimilar materials 1 and 2 with surface energies  $\gamma_1$  and  $\gamma_2$  respectively, the adhesion energy is given by:

$$G_{\text{adhesion}} \approx G_{\text{elastic}} = \gamma_1 + \gamma_2 - \gamma_{12} \quad (1)$$

where  $\gamma_{12}$  is an interaction surface energy and  $G_{\text{elastic}}$  is the mode I energy release rate for crack growth between materials 1 and 2. It is possible to extend adhesion force measurement between two surfaces to the determination of the mode I critical energy release rate. This can be achieved by using theories to link the pull-off force (obtained from AFM experiments) to the adhesion energy.

### 2.4.1 Adhesive Contact Models

#### I. Hertzian Model

The earliest considerations of surface interactions between two dissimilar bodies were captured by Hertz<sup>[70]</sup> in the Hertzian theory of elastic deformation. This theory relates the circular contact area of a sphere with a plane (or in more general cases, between two spheres) to the elastic deformation properties of the materials. Any surface interactions such as near contact Van der Waal's interactions or contact adhesive interactions are neglected. Thus, the Hertzian model does not consider adhesive interactions.

Further theoretical calculations done by Hertz, led him to come up with the following assumptions:

Strains on the contacting solids are small and within elastic limit.

Each solid can be considered as an elastic half-sphere.

The surface are continuous and non- conforming

The surfaces are frictionless.

However in the late 1960's, several contradictions were observed when the Hertz theory was compared with experiments involving contact with spheres of different materials. It was observed that, although Hertz theory applied at large loads, the contact area was larger than that predicted by this theory at lower loads and it had a non-zero value, even when the load was removed . Furthermore, there was strong adhesion if the surfaces were clean and dry. This conclusively indicated that adhesive forces were at work and led to the creation of the Johnson-Kendall-Roberts (JKR) and Derjaguin-Miller-Toporov (DMT) models, which first incorporated adhesion into the Hertzian Contact Model.

## II. Johnson-Kendall-Roberts (JKR) Model

The **JKR**-model for electric contact incorporated adhesion into the Hertzian Contact Model by formulating a theory of adhesive contact using a balance between the stored elastic energy and the loss in surface energy.<sup>[71]</sup> The JKR-model <sup>[72]</sup> considers the effect of contact pressure and adhesion only inside the area of contact.

The general solution for the pressure distribution in the contact area is given by:

(2)

given that ;

(3)

(4)

(5)

(6)

where  $\mathbf{a}$  is the radius of the area of contact  $2\gamma$  is the total surface energy of both surfaces

per unit contact area.

$\mathbf{R}_i$  = Radii of the two contact surfaces

$\mathbf{E}_i$  = Young's Moduli

$\mathbf{v}$  = Poisson's ratio

The approach distance between the two spheres is given by:

(7)

The Hertz equation for the contact area between the two spheres modified to take into consideration the surface energy is:

(8)

Simplifying the above equation(8) with a zero surface energy, returns the Hertzian condition and:

(9)

The **pull-off** force can be described as the tensile load at which the spheres are separated i.e radius of contact area  $\mathbf{a} = 0$  and this force is independent of moduli of the two spheres.

(10)

Another possible solution for the value of  $\mathbf{a}$  at the pull-off load is critical contact area given by

(11)

We earlier defined adhesion energy from the fracture mechanics perspective as:

$$\mathbf{G}_{\text{adhesion}} \approx \mathbf{G}_{\text{elastic}} = \gamma_1 + \gamma_2 - \gamma_{12} \quad (12)$$

The JKR-model radius can thus be written as:

(13)

With the tensile load at separation given as:

(14)

Implying that:

$$(14^*)$$

Where  $\gamma_{JKR}$  is the JKR-model adhesive energy,  $F_{adh}$  is the adhesive force. Equation (14\*) presents the relation between the adhesive force and energy for the JKR-Model. Note that the negative sign denotes opposing sense between the two measured quantities. The JKR model applies to strong adhesive forces between compliant materials with large radii. <sup>[46]</sup>

### III. Derjaguin-Muller-Toporov (DMT) Model

The DMT-model can be used to characterize weak interactions between stiff materials with small radii. <sup>[46]</sup> The DMT model <sup>[73][74]</sup> developed an alternative for adhesive contact by assuming that the contact profile remained the same as in the Hertzian contact, but with additional attractive interactions outside the area of contact. The Hertz equation for area of contact between two spheres from the DMT theory is:

$$(15)$$

The **pull-off** force is

$$(16)$$

When the pull off force is achieved, the contact area becomes zero and singularity in the

contact stresses at contact area edges ceases to exist, in terms of work of adhesion ,

$$(17)$$

$$(18)$$

and 
$$(19)$$

Hence, Equation (19) is the relation between the adhesion surface energy and adhesion force for the DMT-Model.

#### IV. Maugis-Dugdale Model

Apparent contradictions between the earlier **JKR** and **DMT** theories were resolved by noting that the two theories were the extreme limits of a single theory.<sup>[75]</sup> The JKR theory applied too large compliant spheres while the DMT applied very small stiff spheres. As such D. Tabor<sup>[76]</sup> in 1977, resolved the issue of contradiction by introducing a coefficient know as the Tabor coefficient  $\mu$  to harmonize the differences.

$$\mu := \frac{d_c}{z_0} \approx \left[ \frac{R(\Delta\gamma)^2}{E^{*2} z_0^3} \right]^{1/3} \quad (20)$$

where  $z_0$  is the equilibrium separation between the two surfaces in contact. However further improvements to Tabor's idea were made by D. Maugis.<sup>[77]</sup> Surface force was represented in terms of Dugdale cohesive zone approximations, such that the work of adhesion is given by:

$$\Delta\gamma = \sigma_0 h_0 \quad (21)$$

where  $\sigma_0$  is the maximum force predicted by the Lennard-Jones potential and  $h_0$  is the maximum separation obtained by matching the areas under the Dugdale and Lennard-Jones curves.<sup>[76][80]</sup> After this point, the constant adhesive force,  $\sigma_0 = 0$ .

For the MD model that lies between two limiting cases, analytical methods are used to obtain the exact relationship between adhesion force and energy. It is a much more complex theory but is simplified using an iterative process developed by Carpick-Ogletree-Salmeron<sup>[79]</sup> (COS) model. It also requires a combination of material and geometric properties.

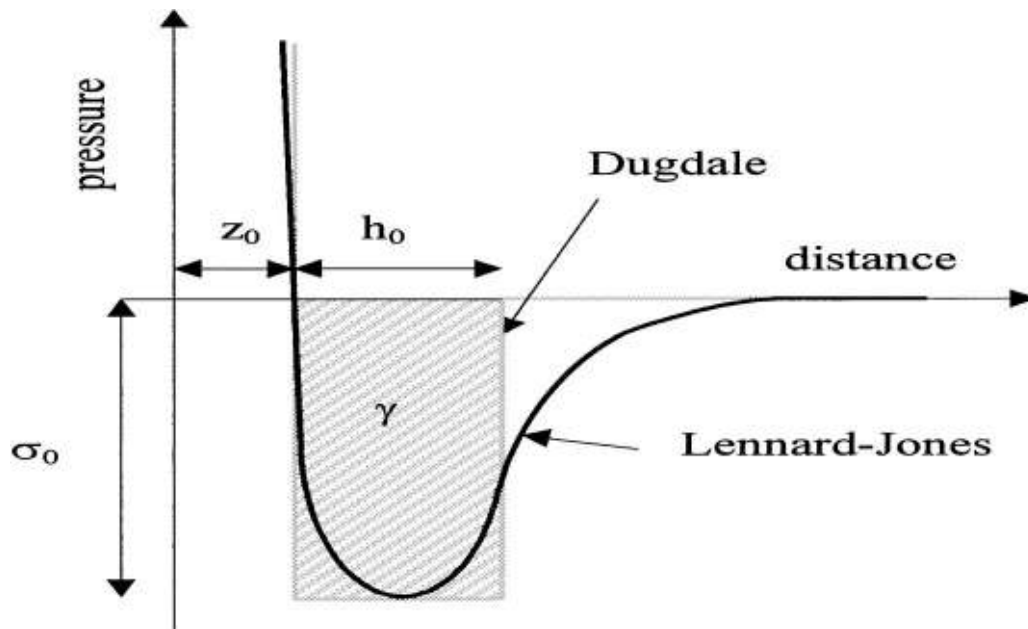


**Fig. 2.7: Lennard–Jones and Dugdale surface force laws.**<sup>[80]</sup>

(In the Dugdale case, the adhesive force is assumed to have a constant value  $\sigma_0$  until a separation  $h_0$  is reached, where it falls to zero. The value  $h_0$  is chosen in order to match the work of adhesion corresponding to the Lennard–Jones potential.)

The advantage of this model however is that it can be used to characterize the entire range of adhesion models earlier discussed through the calculation of a dimensionless parameter  $\lambda$ .

where

$$\lambda = 2\sigma_0 \left( \frac{R}{\pi K^2 \gamma} \right)^{1/3} = -0.913 \ln(1 - 1.018\alpha) \quad (22)$$

where  $\alpha$  is a transition parameter

Given that, effective radius R is given by:

$$R = \left( \frac{1}{R_{\text{tip}}} + \frac{1}{R_{\text{rms}}} \right)^{-1} \quad (23)$$

and the constant K is expressed as:

$$K = \frac{4}{3} \left[ \frac{(1 - \nu_1^2)}{E_1} + \frac{(1 - \nu_2^2)}{E_2} \right]^{-1} \quad (24)$$

The adhesion energy can itself be found from:

$$\gamma = \frac{G}{2} = \frac{F_{\text{ad}}}{\pi R F_{\text{ad}}} \quad (25)$$

$$\bar{F}_{\text{ad}} = 0.267\alpha^2 - 0.767\alpha + 2 \quad (26)$$

The JKR theory exists when values of  $\lambda > 5$ ; For values of  $\lambda < 0.1$  correspond to the DMT model. The intermediate case where  $0.1 < \lambda < 5$  corresponds to the MD model. The expressions for pull-off forces can be used in obtaining values for the adhesion energy over a wide range cases.

## 2.5 Charge Transport in OLEDs and HOILEDs

### 2.5.1 Introduction

This section describes the nature of electron and hole transport between different layers of the OLEDs and HOILEDs structure. The charge transport is the same for both devices and “**field emission**” via **tunneling** is used for this description since I-V are field dependent characteristics rather than voltage dependent. Another form of charge transport is the **Schottky barrier** which will be briefly discussed as it does not apply to organic LEDs but photo-voltaic cells, transistors and inorganic diodes.

### 2.5.2. Fowler-Nordheim tunneling

#### Field Emission

This is the emission of electrons from a metal or semiconductor into vacuum open air or other media when induced by an external electromagnetic field strength  $E$ .<sup>[82]</sup> It can also occur from solid and liquid interfaces or between individual atoms which result in transportation of electrons from one layer to another.

In field emission, electrons tunnel through a potential barrier rather than escaping over it as in photo-emission or thermionic emission. The effect is purely quantum-mechanical with no classical input. The wave function of an electron does not vanish at the classical turning point, but decays exponentially into the barrier and there exists a finite probability that electrons would be found outside the barrier. In a metal for example, the metal can be considered to be a potential box filled with electrons at the Fermi level. The vacuum level represents the potential energy of an electron at rest outside the metal with no applied external field  $E$ . When the field is applied, the potential outside the Fermi level forms a triangular barrier where charge tunneling occurs. Cold emission is normally used to describe emission of electron from a solid or liquid conductor under the influence of a high electric field.

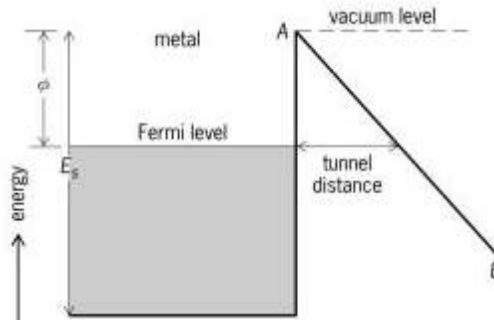


**Fig.2.8: Diagram to illustrate charge tunneling with energy level scheme**

A strong electric field lowers the barrier and makes it sufficiently penetrable. That is relatively thin and low.<sup>[82]</sup> Field emission is sometimes called AUTO ELECTRONIC EMISSION because energy is not expended to excite electrons. R. Milikan and C. Lauritsen<sup>[83]</sup> established that the logarithm of the field emission current density  $\hat{J}$  is linearly dependent on the reciprocal of the electric field. Field emission was later explained on a quantum-tunneling basis in a theory proposed by Fowler and Nordheim<sup>[86]</sup> via some family of equations named after them. Fowler and Nordheim equations apply only to field emissions from bulk metals and with suitable modifications to other bulk crystalline solids. They are also used as a rough approximation to describe field emission in other materials. Simple solvable models of the tunneling barrier leads to complex equations which will not be discussed in detail in this thesis. Fowler-Nordheim predicts that;

$$I = E^2[\exp(-K/E)] \quad (27)$$

where I is the current , E is the electric field strength, K is the parameter that depends on

geometry of barrier. Hence, in the case of Fowler-Nordheim tunneling, a plot of  $\ln(I/E^2)$  versus  $1/E$  produces a linear plot, particularly at very high field strengths. The deviation from linearity at lower fields probably indicates an additional contribution to current thermionic emission, which is frozen out at lower temperatures.<sup>[84]</sup> If we assume that the injected charge is tunneling through a triangular barrier at one of the polymer interfaces, the constant  $K$  in equation (27) is given by:

$$\kappa = \frac{8\pi(2m^*)^{1/2}\Phi^{3/2}}{3qh} \quad (28)$$

where  $\Phi$  is the barrier height,  $m^*$  is the effective mass of the electron.

By analysing “electron and hole-only” devices, it is observed that both charges are injected into the polymer layer for recombination by tunneling technique. The field emission current density  $\hat{J}$  is part of the flux density  $\mathbf{n}$  of electrons incident on the barrier from inside the conductor and is determined by the transmission coefficient  $\mathbf{D}$  of the barrier.

$$j = e \int_0^\infty n(\delta) D(\delta, E) d\delta \quad (29)$$

here,  $\delta$  is the fraction of the electron's energy that is associated with the component of momentum normal to the surface of the conductor,  $\mathbf{E}$  is the electric field strength and  $e$  is the electronic charge.

### 2.5.3. Schottky Barrier

A Schottky barrier is a potential barrier that is formed in the contact region of a semiconductor and metal under equilibrium. To obtain a Schottky barrier, the work function of metal and semiconductor must differ. The Schottky barrier is an electron or hole barrier

caused by an electric dipole charge distribution associated with the contact potential difference. Hot carriers (electrons and holes for n- & p-type materials, respectively) are emitted from the Schottky barrier of the semiconductor and move to the metal coating, since majority of carriers predominate, there is essentially no injection or storage of minority carriers. If the semiconductor is p-type, holes experience the same type of potential barrier but, since holes are positively charged, the polarities are reversed from the case of the n-type semiconductor. In both cases, the applied voltage of one polarity (called forward bias) can reduce the potential barrier for charge carriers leaving the semiconductor, but for the other polarity (called reverse bias) it has no such effect.<sup>[81]</sup>

## **2.6 Earlier research work and contributions to present OLED technology**

The first organic light emitting device was reported at Eastman Kodak by Ching W. Tang and Steven Van Slyke in 1987 . The device used a novel two-layer structure with separate hole and electron transporting layers, such that the recombination and light emission occurred in the middle of the organic layer.<sup>[26]</sup> This resulted in an operating voltage reduction and improved efficiency, eventually leading to the current era of OLED research with novel fabrication designs.

Borroughes et al.<sup>[27]</sup> later continued with research into polymer electro-luminescence at the Cavendish laboratory in 1990. This was done to obtain a high efficiency green-light emitting polymer-based device using 100-nm thick films of poly(p-phenylene-vinylene) (PPV).

Since then, significant progress has been made in the field of organic electronics. The performance of OLED devices has been shown to be largely dependent on properties of individual layers and interfaces which dictate charge-injection, charge transport and charge recombination properties.<sup>[28]</sup>

Hence, significant efforts have been made to modify the interfaces by introducing multiple thin-layers into the main structure to maximize performance. <sup>[28][29][30][31][32]</sup>

For example, Zhan et al.<sup>[7]</sup> have used charge carriers as a means of increasing the efficiency of OLEDs. A 10-nm thick layer of PBD was inserted between the NPB organic layer and the Alq<sub>3</sub>-electron transport layer (ETL). The PBD improved the device stability and efficiency by serving as a protection layer to reaction with external factors (air), while serving as a hole-buffer layer (HBL) to absorb the excess holes transported through the organic layer (O.L.) from the ITO anode. In this way, the overall device performance and life span is optimized.

The effect of introducing ETL of 2,7-bis[2-(4-tert-butylphenyl)-1,3,4-oxadiazol-5-yl]-9,9-dihexylfluorene (DFD) into MEH-PPV polymer blend has been studied by Ana et al. <sup>[32]</sup>. DFD contains both oxadiazole and fluorene units to confer electron injection and provide blue emission respectively. The results show that the light output increased for some concentration of DFD blends and decreased with further addition. In general, the incorporation of DFD electron transport material increased device efficiency by two-orders of magnitude ( $10^{-3}$  % - 0.1%).

Weng et al. <sup>[66]</sup> have also worked on electro luminescence of MEH-PPV/TiO<sub>2</sub> composites in which TiO<sub>2</sub> nano-needles were introduced into the polymer. The rutile TiO<sub>2</sub> was chosen due to its chemical stability and high aspect ratio. This easily forms a percolation network within the polymer thereby influencing hole and electron transport in the device.

The results showed a 2.8-fold enhancement in the normalized integrated area of EL with 5 wt% TiO<sub>2</sub> nano needles in MEH-PPV. This enhancement was due to decrease in hole barrier height and the increase in hole mobility.

With OLEDs, the injection efficiency of electrons is a critical parameter and depends to a great extent on the work function of the electrode. Yuan et al. <sup>[39]</sup> in their recent work have suggested introducing an anode-buffer layer (ABL) or metal phthalocyanine (MPc) of Li-

doped zinc-oxide (LZO) between the anode and organic layer. The results thus revealed an enhanced hole-injection which resulted in a desirable decrease of turn-on voltage from 5.3V to 4.3V. However, the origin of the improved turn-on voltage was attributed to the reduction of injection barrier at the ITO/NPB (organic) interface.

This idea can be also applied to the development of high efficiency white OLEDs with lower turn on voltages and high power efficiencies which will advance commercialization of lighting emitting devices.

Doping of the emitting layers of OLEDs ( $\text{Alq}_3$  mostly) with wide band-gap impurities like 4,4-bis(2,2-diphenylvinyl)-1,1-biphenyl (DPVBi) also increases stability.

Using a  $30\Omega/\text{sq}$  resistivity ITO with the necessary layers deposited, analysis by Choo et al.<sup>[8]</sup> revealed that an introduction of DPVBi layer decreased the Trap-charge limited current (TCLC), thereby increasing the amount of electrons transported through the emitting layer (EML), giving a higher current density. This enhances the overall lifetime of the OLED.

Saba and Farhad analyzed the degradation of OLEDs in which PEDOT: PSS organic layer have been spin coated onto an ITO-sputtered glass substrate. The electrical characterization revealed an exponentially decreasing trend in the current versus time plot.<sup>[35]</sup>

Akande et al.<sup>[37]</sup> have also studied instabilities in polymer light emitting devices using a model based on spontaneous ordering of the thin-film system. Analysis of the growth of blisters and bubbles was done by noting the interplay between the operational stresses as a result of Joule heating and the equilibrium residual stresses due to properties of the device as higher threshold voltages are required for operation. Thus, providing a means of inhibiting growth of these blisters is likely to enhance device efficiency.

Analysis of layer modification of different of individual OLED layers is also an area of intense worldwide research.<sup>[37-39]</sup> Furthermore, recent studies have also explored the potential effects of replacing electrode layers with other materials that can improve the luminance efficiencies and device stabilities.

Barry et al.<sup>[37]</sup> have replaced the commonly used and expensive Indium tin-oxide (ITO) with less expensive Gallium-doped Zinc-oxide (GZO). A better sheet resistance ( $R_s$ ) and transparency was observed in GZO relative to ITO anode. Furthermore, device data suggested GZO effectively injecting holes into the HTL and an improved OLED stability was attained at lower cost per unit area.

In another article, Wu et al.<sup>[38]</sup> retained the ITO anode but improved its contact characteristics via plasma treatment. It was seen from experimental results that an enhanced hole injection efficiency improves the operating voltage from greater than 20V to less than 10V, with the electro luminescence quantum efficiency increasing by a factor of 4 (0.28%-1.0%).

A much higher drive current was applied to achieve much higher brightness ( $\sim 10,000$  cd/m<sup>2</sup> at 1000 mA/cm<sup>2</sup>). Hence, as a result, the lifetime of the device increased by two orders of magnitude.

Huang et al.<sup>[39]</sup> have used a more complex multilayer anode composed of Aluminum and Gold (Al/Au). The Al/Au anode layer was selected due to its high reflectance and low work function properties. These aid efficient hole injection into a varying organic layer thickness. Also, for an optimized thickness, a balance in electron and hole recombination ratio was achieved. This consequently produced a device with brightness and luminance efficiency of 8.041 cd/m<sup>2</sup> and 3.0 cd/A respectively .

However, in spite of the significant progress that has been made in OLED research, there are relatively few applications of OLEDs in commercial devices. There is, therefore, a need for additional research. There is also a need to develop a basic and applied understanding of hybrid organic -inorganic light emitting devices with the potential for future applications.

Most of the early works on HOILEDs have used inorganic oxides as carriers.<sup>[39][44]</sup> The operating mechanism of carrier injection in hybrid organic-inorganic LEDs (HOILEDs) has been analyzed by Katsuyuki et al.<sup>[40]</sup> A fascinating behaviour was revealed at the interface

between the organic layer and metallic oxide layer. A unique interaction between the MoO<sub>3</sub> and poly(dioctylfluorene-alt-benzothiadiazole) [F8BT] caused a hole injection enhancement in the HOILED with a corresponding large number of electrons extracted as a result of the injected holes.

Bolink et al.<sup>[45]</sup> have used an air insensitive cathode (due to its relative air stability) while incorporating metallic oxides into the light emitting polymer. With this configuration, much higher brightness was achieved, reaching 6500 cd/m<sup>2</sup> and voltages as low as 8V. Compared to conventional devices, this device operates in air for a longer time.

The existent degradation problem in organic light emitting devices can be analyzed from the charge carrier perspective. The better the adhesion energy between materials used for the different layers, the more efficient the charge transport across layers and as such, device enhancement can be studied. Adhesive forces and surface energies at the nano scale level existing between layers of organic electronic structures has been studied by Tong et al.<sup>[46]</sup> The results of Atomic Force Microscopy (AFM) measurements of adhesion between layers were examined carefully in this study.

## CHAPTER THREE

### 3. Characterization and Adhesion Analysis in OLEDs and HOILEDs

This chapter provides a detailed explanation of the different characteristics of individual thin-film layers on glass. These include ITO and those of complete devices fabricated when an Aluminium Cathode is deposited on polymer layers spin-coated on ITO-coated substrate. Adhesion analysis is also carried out on each interacting layer before relating the adhesion to the measured optoelectronic properties.

#### 3.1 Experimental Methods

A detailed description of the fabrication procedure for each thin-layered structure and device configuration is provided in this section.

##### 3.1.1 Materials

All chemical compounds purchased for preparing the thin-film layer samples and devices were of very high purity with the polymer solutions prepared in the laboratory just before use.

Chemicals used for cleaning glass slides and shadow masks are as follows.

Decon-90

Acetone  $\text{CH}_3\text{COCH}_3$

Ethanol  $\text{C}_2\text{H}_5\text{OH}$

De-ionized water (DI)

Neutracon

Different equipment used for deposition, cleaning, weighing, annealing and other experimental processes required for the successful analysis include.

VWR ultrasonic cleaner

Carbolite heating oven (Model 301, Carbolite Group, Wisconsin)

Dessicator

KIKA Labortechnik Magnetic stirrer

Ainsworth weighing scale

Keithley Set-up for Electrical Characterization (consisting the Four-point probe and DC Source Meter)

Veeco Profiler

EVD Scanning Electron Microscope (SEM)

UV/Vis Spectrophotometer

Edward Auto 306 Thermal Evaporator

Edwards Auto 306 RF Magnetron Sputtering Machine

Laurell Spin Coater (WS-650HZ Model)

Nitrogen gun

### **3.1.2 Deposition of ITO Thin-Film layer on glass Substrate and AFM tips**

There are four steps to the preparation of ITO thin-film layer on glass and AFM tips prior to their general characterization.

These include:

Cleaning of glass slides

Preparation of AFM tips

Deposition of Indium-Tin oxide by sputtering

Annealing of ITO thin-film layer

#### **3.1.2.1 Cleaning of glass slides**

Organic light emitting device fabrication requires very clean atmosphere to prevent

contamination of the components that affect device operation. As such, the cleaning of materials used in the fabrication process is very essential. First the glass slides were cut into 2.5 cm x 2.5 cm (approx. 1 sq inch) squares. The surfaces of the glass slides were then rinsed carefully in de-ionized water. Subsequently the slides were washed thoroughly in Decon-90 and re-rinsed in de-ionised water before soaking in acetone. They were then placed in an ultrasonic cleaner and cleaned for 10 minutes at room-temperature. The samples were then removed from the cleaner and rinsed with ethanol with further blow-drying using Nitrogen gas from a Nitrogen gun. Figure 3.1 shows the ultrasonic cleaner that was used for cleaning.

### **3.1.2.2 Preparation of AFM tips**

The tips were delivered in a black casing glued to some silicon base. They were carefully removed using clean tweezers and placed on a 25 x 25 cm<sup>2</sup> glass slide using a double-sided tape. Care was taken to ensure that the tips did not break during placement and mounting into the sputtering chamber for coating with ITO.

### **3.1.2.3 Deposition of Indium Tin-Oxide by Sputtering.**

Indium Tin-Oxide was sputtered onto clean glass slides using an Edwards R.F. Magnetron Sputtering system that was operated at an initial vacuum pressure of  $4.0 \times 10^{-5}$  Torr and R.F. power of 40 W. The sputtering was carried out at room-temperature (RT). Argon was introduced to excite ions on the ITO target, thereby starting the deposition process with an initial deposition rate of 0.12 Å/s being set on the screen. A nominal thickness of 100 nm of ITO was coated onto glass after about 80 minutes, with an average deposition rate of 0.80 Å/s and final pressure of  $3.2 \times 10^{-3}$  Torr. The increase in sputter power increases the rate of deposition of ITO atoms to the glass surface. The set-up that was used for the sputtering

process is shown in **Fig 2.4** along with a circular window that was used to monitor the deposition process.

#### **3.1.2.4 Annealing of ITO Thin-Film layer and AFM tips**

The process of annealing discussed earlier in Section 2.3.2.1, was carried out to reduce the Sheet resistance,  $R_s$ , of the ITO-coated glass samples. These samples were annealed in a Carbolite oven (Model 301, Carbolite Group, Wisconsin) at 250° C for an hour. The Carbolite oven is shown in **Fig. 3.3**. This changed the structure of the ITO from an amorphous to crystalline structure. The resulting samples were then labelled as  $A_{II}$ ,  $A_{III}$ .... Sample  $A_I$  was reserved as an unannealed control sample for comparison.

#### **3.1.3 Deposition of PEDOT:PSS Thin-Film layer on glass substrate and ITO-coated glass**

The PEDOT:PSS was obtained from Princeton, USA in liquid form, already prepared as PEDOT:PSS solution. Filtration was then carried using a 0.25  $\mu\text{m}$  mesh size filter paper to ensure a smoother layer when spin coated, since the PEDOT:PSS layer acts as a smoothing layer and hole transport layer (HTL). The PEDOT:PSS was spin coated using a Laurell Spin coater with a Program Recipe set on the machine. By smearing the glass surface with several drops of polymer solution in a static dispense mode, the substrate is rotated at moderately-high speed (1500 rpm) in order to spread the polymer by centrifugal force. Further rotation is achieved at higher speeds (2000 – 3000 rpm) for 60 seconds, with fluid being spun off the edges of the glass and thinning-out of the film until the desired film thickness of ~ 100 nm was achieved. The Spin Coating recipe is shown in **Table 3.0** with parameters that affect the characteristics of the film. The spin coated samples were dried in an oven for 10 minutes before labelling them as Samples B and C for glass and ITO-coated glass respectively.

### 3.1.4 Deposition of MEH-PPV Thin-film layer on Glass and ITO-coated glass

The two stages in the preparation of the MEH-PPV thin-film (prior to the characterization of individual layers) involve:

the preparation of MEH-PPV polymer Solution, and

the spin coating of MEH-PPV solution on glass and ITO-coated glass

#### 3.1.4.1 Preparation of MEH-PPV Polymer Solution

Poly(2-methoxy-5-(2'-ethylhexyloxy)-1,4-phenylenevinylene) (MEH-PPV) solute particles were dissolved in chloroform solvent using a mass to volume ratio of 100 mg of solute in 20 ml of solvent. This resulted in an orange-red solution. The first step involved mixing of the polymer and solvent in a 200 ml conical flask prior to stirring for 6 hours using a KIKA Labortechnik Digital Magnetic stirrer shielded from light. The orange-red solution was protected from light to prevent any reaction and stirred rigorously between 600 rpm to 1000 rpm. The final solution was filtered with 0.25  $\mu\text{m}$  mesh-size filter paper, prior to spin coating. **Fig. 3.2** shows the filtered solution of MEH-PPV just before it is spin coated on glass. (**NOTE: stirring was carried out under dark conditions, cover was removed to take**



this picture)

**Fig 3.1: MEH-PPV in 25ml beaker during stirring at 695rpm**

**Fig 3.2: MEH-PPV after filtration and ready for spin coating**

Sample	Substrate & Size	Cleaning	Scope	Material/Reagent	Volume Dispensed (ml)	Syringe volume (ml)	Expected thickness
PEDT-1	2.5x2.5	Normal	Device	PEDOT:PSS	0.4	2	100 nm
<b>PROGRAM:</b>					Baking Temp. °C	Baking time	
5					100	10 mins	
Step No.	Duration (sec)	Speed (rpm)	Acceleration (rpm/s)	Dispense	Comments		
1	5	1500	100	Static			
2	3	1500	1000				
3	60	3000	1500				

**Table 3.0: Spin Coating Recipe**

### 3.1.4.2 Spin Coating of MEH-PPV on glass and ITO-coated glass

During spin coating, the glass slides were placed on the spinning chuck of the Laurell spin coating system (shown in **Fig. 2.5**). they were then held down by a vacuum pump before applying several drops of MEH-PPV to cover 80-90% of the glass slide. The spin coating was then carried out using conditions that were entered into the program recipe (**Table 3.2**). After spin coating, the glass slides were placed in an oven at 100 °C. This was used for drying to remove any excess solvent from the glass surface.

The same procedure was carried on the ITO-coated glass samples fabricated in Section 3.1.3. However, an Al-cathode layer was also deposited using evaporation techniques that will be discussed in detail later. Thickness of individual layers of polymer material was achieved by several spin coating dummy tests carried out and tested with the Veeco Profiler, until the desired thickness of ~ 150 – 200 nm was achieved. The samples were placed in sample cases and labelled D and E.



**Fig. 3.3: Carbolite Oven used for annealing and drying samples**

### **3.1.5 Deposition of Aluminum thin-film on glass substrates**

The main technique for depositing the Al thin-film layer is by thermal evaporation of Aluminium onto clean glass substrates. The apparatus for thermal evaporation is shown in **Figure 2.6** and detailed explanation of the deposition technique is discussed in Section 2.3.4. A pure Aluminium rods (99.9%) of about 1cm radius and length was placed on a tungsten filament in the evaporation chamber. This was melted in a high vacuum ( $2.0 \times 10^{-5}$  Torr) environment. Rate of deposition and thickness were controlled using the Inficon Deposition controller. The Al was then evaporated and coated through a shadow mask onto the glass slide. The samples were tagged as sample F.

### **3.1.6 Deposition of MEH-PPV+TiO<sub>2</sub> hybrid layer**

The main reason for fabricating this unique layer is to analyse the adhesion of MEH-PPV+TiO<sub>2</sub> to glass (MEH-PPV+TiO<sub>2</sub>/Glass) and its adhesion to PEDOT:PSS (MEH-PPV+TiO<sub>2</sub>/PEDOT:PSS). The MEH-PPV was prepared with the same mass to volume ratio described in Section 3.1.4. In this case, 15 mg of MEH-PPV was dissolved in 3 ml of chloroform with 5 mg of TiO<sub>2</sub> nano particles to give a hybrid blend. This was then spin coated onto glass and ITO-coated glass.

### **3.1.7 Fabrication of Organic Light Emitting Device**

Device fabrication was carried out after close analysis of each layer that makes up the device. After sputtering ITO on glass, the ITO-coated glass samples were coated with PEDOT:PSS which acts as a Hole Transport Layer (HTL) and a smoothing layer for the ITO. MEH-PPV was subsequently spin coated on to serve as a light emissive area (Active area). The MEH-PPV also serves as an Electron Transport Layer (ETL) to aid the injection of electrons into the active recombination zone. This was done with the same spin coating parameters described for the deposition process of the MEH-PPV onto the ITO layer. Thermal evaporation of the Al-Cathode layer was carried out using the Edwards Aut0 306 Thermal evaporator (Edwards, UK) at a high voltage (10 V) and a high vacuum ( $2.0 \times 10^{-6}$  Torr).

### **3.1.8 Fabrication of Hybrid OLEDs**

Fabrication of the hybrid organic-inorganic LEDs (HOILEDs) followed the same trend as the fabrication of the OLEDs. However, in this case, the active layer consisted of TiO<sub>2</sub> nano particles mixed with MEH-PPV. HOILEDs when fabricated, were relatively more stable than their organic LEDs counterparts.

## **3.2 Thin-Film Layer and Device Characterization**

### **Introduction**

This section describes the different types of characterization techniques that were used to study the thin-film layered structures and organic/hybrid organic-inorganic light emitting devices (OLEDs/HOILEDs).

### 3.2.1 Surface Morphological Characterization

The deposition technique with suitable deposition parameters adopted during thin-film analysis greatly determines the properties of the final surface. The most important properties of a particular layer when considering OLEDs and HOILEDs is the layer roughness and thickness. The easiest means of determining this is using the surface profiler which makes use of extremely sensitive diamond tip to probe the surface of the layer. The high aspect ratio tips are ideal for measuring shallow depths, trenches, or non-uniformities on the layer surface to the level of  $10^{-10}$  m (Angstrom units).

The Veeco Dektak 150 Surface Profiler was used for surface characterization of the different layers that make up the OLED/HOILED. By way of a moving stage right under the tip, samples are analysed according to parameters set in the scan routine of the program used for probing. These include; scan length, scan time and scan resolution. The profiler tip combined high repeatability with a low-force sensor on the surface of the thin-films. This was used to measure accurate values for step heights, surface roughness and waviness. It provides a basis for characterization of the different layers. The layer configurations that were characterized include: ITO/Glass, PEDOT/Glass, PEDOT/ITO/Glass, MEH-PPV/Glass, MEH-PPV/ITO/Glass, MEH-PPV+TiO<sub>2</sub>/Glass and MEH-PPV+TiO<sub>2</sub>/ITO/Glass.

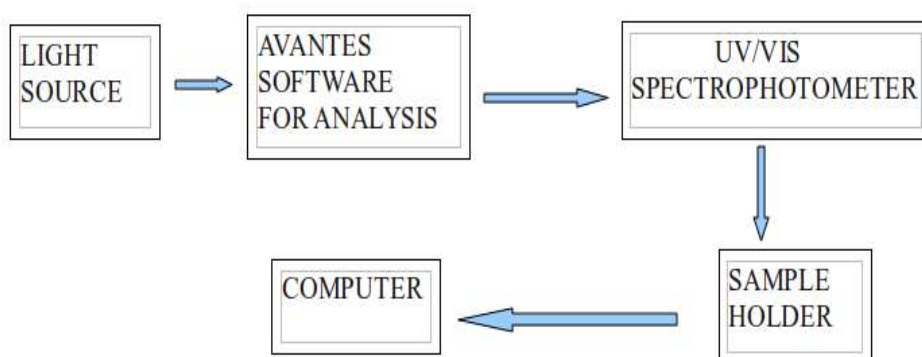


**Fig. 3.4: Schematic for Optical characterization**

### 3.2.2 Optical Characterization

This section describes the optical characteristics (of the different individual layers that make up the complete organic device) that were characterized using a UV/Vis AvaSpec 128 Fibre-Optic Spectrophotometer (Avantes BV, USA). Further characterization of the light emitted from the working device was carried out by observing the electroluminescence with an optical fibre that was used to capture almost all the light in a dark room.

Organic layers are known to emit light when voltage is applied across electrodes that sandwich them. For the transmission spectra study, thin films of different substances were deposited on glass and ITO-coated glass. The optical properties were then studied using a UV/Vis Spectrophotometer consisting of a light source and detector, all connected by optical fibre. Optical characterization of light emitted from the complete device (OLED), during the application of a forward bias voltage, involved placing the fibre detector close to the window of the test fixture in which the device was mounted. To capture as much light as possible and to prevent interference from other light sources, the whole process was carried out in a dark room. The shape of the device did not allow the use of an integrating sphere for analysis as the device was much larger than it. The set-up for the optical characterization is shown in **Fig. 3.4**. The layer configurations listed in Section 3.2.1 were characterized here.

### 3.2.3 Adhesion Measurements with Atomic Force Microscopy

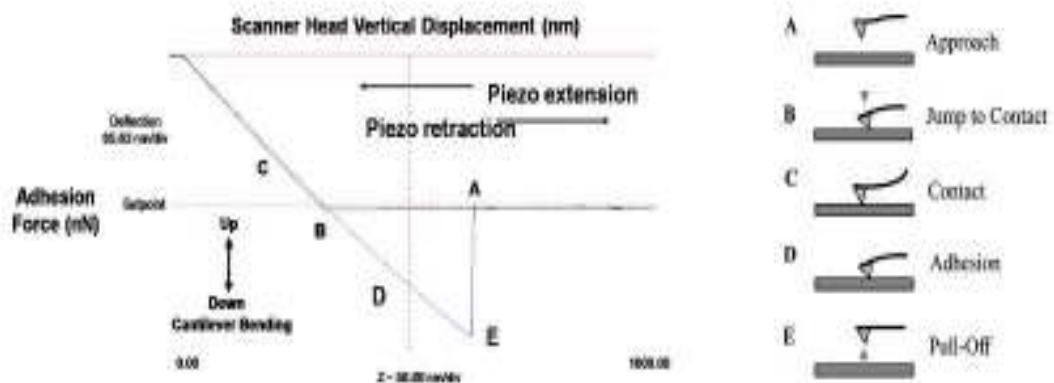
This section describes the procedure by which adhesion measurements were carried out for the possible bi-material pairs in the model OLED and HOILED structures described here. These measurements were carried out at the Princeton Laboratory by Tiffany Tong in the Soboyejo laboratory. These results will be compared to the optoelectronic properties of the layers and devices that were obtained at SHESTCO laboratory.

In the contact mode, Atomic Force Microscopy (AFM) was used to measure the pull-off forces  $F_{\text{pull-off}}$  between thin-film layers. AFM tips coated with the required complementary

material were used, while the other layer was coated to glass depending on the particular adhesion analysis. A dip coating technique developed by Zong et al.<sup>[82]</sup> was used for polymer coating of the tips, when comparing the adhesion between the polymer layers (e.g. PEDOT:PSS/MEH-PPV, PEDOT:PSS/MEH-PPV+TiO<sub>2</sub> layers).

First, the micro fabricated cantilever probe was attached to a scanner head and lowered to the thin-film surface at constant velocity under ambient conditions of temperature (25 °C) and humidity (40 - 50%). Negligible interaction were experienced by the tip with the surrounding medium during the early stages of tip deflection. However, as the tip is lowered further down, it is eventually pulled into contact by adhesive force interactions with the surface of the substrate layer. There tip then bends elastically as it is further displaced in the downwards direction. Upon reversal of the displacement direction, the bending is reversed but the tip does not detach at zero force, due to adhesive interaction. Hence, a negative force (load) is required to pull-off the tip at point E in Fig. 3.5. This is known as the **pull-off** force. Using Hooke's law and adhesion models presented earlier in Chapter Two, force-displacement characteristics and adhesion energies were determined. An example of a typical force-displacement curve is presented in **Fig. 3.5**. The figure also includes schematic

i



ations of the different stages of the AFM adhesion experiments.

**Fig. 33.5: Schematic force-displacement curve depicting the various stages of cantilever-surface engagement**<sup>[46]</sup>

### 3.2.4 Electrical Characterization of Layered Structures and Device

This section describes the electrical characteristics of the individual layers. These were determined by finding the Sheet Resistance,  $R_s$  of the different layers using a Keithley set up consisting of a Four point probe system that essentially measures this property. The layered samples were placed on the base of the device and the probe lowered to interact with their surfaces. Measurements of sheet resistance and thickness of each layer can be measured using this device, Comparison of the sheet resistance  $R_s$  with the roughness averages from the surface profiler presents an interesting result.

For a very thin layer of thickness  $t$ , the resistivity is given by:

$$\rho = \frac{\pi t}{\ln 2} \left( \frac{V}{I} \right) \quad (30)$$

where  $t$  is the sheet thickness,  $V$  is the applied voltage/bias, and  $I$  is the current. Note that where the probe spacing  $s \gg t$ , we take the general sheet resistivity to be  $\rho/t$ . As such, the sheet resistivity is given by:

$$R_s = k \left( \frac{V}{I} \right) \quad (31)$$

where  $k$  is  $\pi/\ln 2 \approx 4.532$

Values of sheet resistance were thus obtained for the various layers. Further electrical characterization of the device was done using the DC Source Meter which is also part of the Keithley set-up. This was used to measure Current ( $I$ ) – Voltage ( $V$ ) characteristics as a function of time. The time-dependent measurements were used to characterize device degradation in air. The Keithley set-up, consisting of a DC Source Meter and a Four point

probe system that was used to characterize the device is shown in **Fig. 3.6**.



**Fig. 3.6: Keithley Set-Up for Electrical Characterization**

The Source Measurement Unit (SMU) was connected in such a way that the SMU for current was in the sweep mode between 0 to 20 mA with a delay of 500 milli-seconds.

Using the Keithley set-up, the DC power supply was turned on. The red Clips were then connected to the ITO anode, while the black clips were connected to the Al cathode. An initial current of 20 mA was set in the sweep mode to observe any illumination from the active area of the device. The circuit configuration for the device I-V characterization is presented in **Fig. 2.0**.

### 3.3 Results and Discussions

#### 3.3.1 Surface Morphological Characterization of Thin-Film Layers

The results of the surface profilometry measurements of films deposited on glass and ITO coated glass are presented in Fig. 3.7 - Fig. 3.17. These show the thicknesses and roughness profiles for the different layers. The roughness is denoted by a roughness-average value  $R_a$  and differences are apparently visible from the height and phase scans (Table 3.1). The lowest roughness average of ITO thin film on glass ( $0.72 \pm 0.01$  nm) shows a good deposition of anode from the sputtering process. The majority of the layers have roughness average values within reasonable limits, when compared to the actual thickness of the deposited layer. The SEM images (Fig. 3.18- Fig. 3.21) also confirm the results from the profiler. For example, MEH-PPV layer on glass (Fig. 3.20), as compared to the ITO image (Fig.3.18) confirms the nature from its SEM images. PEDOT:PSS on ITO heated at  $250^\circ\text{C}$  did not vary in its surface morphology when compared to PEDOT:PSS dried at the required  $120^\circ\text{C}$  (Figs. 3.16 and 3.17). This test was carried out to analyse the effect of high temperature on the PEDOT:PSS/ITO layer. The roughness data obtained for different layers which make up the device enables a better selection of materials combination in devices where a wide range of materials are being considered for numerous applications.

Layered structure	Roughness average $R_a$ (nm)	Thickness (nm)
ITO on glass	0.72	100
PEDOT:PSS on glass	3.47	100
PEDOT:PSS on ITO (heated at $100^\circ\text{C}$ )	3.9	100
PEDOT:PSS on ITO (heated at $250^\circ\text{C}$ )	3.58	100
MEH-PPV on glass	11.69	110
Hybrid MEH-PPV	19.0	150
Aluminum on glass	1.7	200

**Table 3.1: Roughness average and thickness for different layered structures**

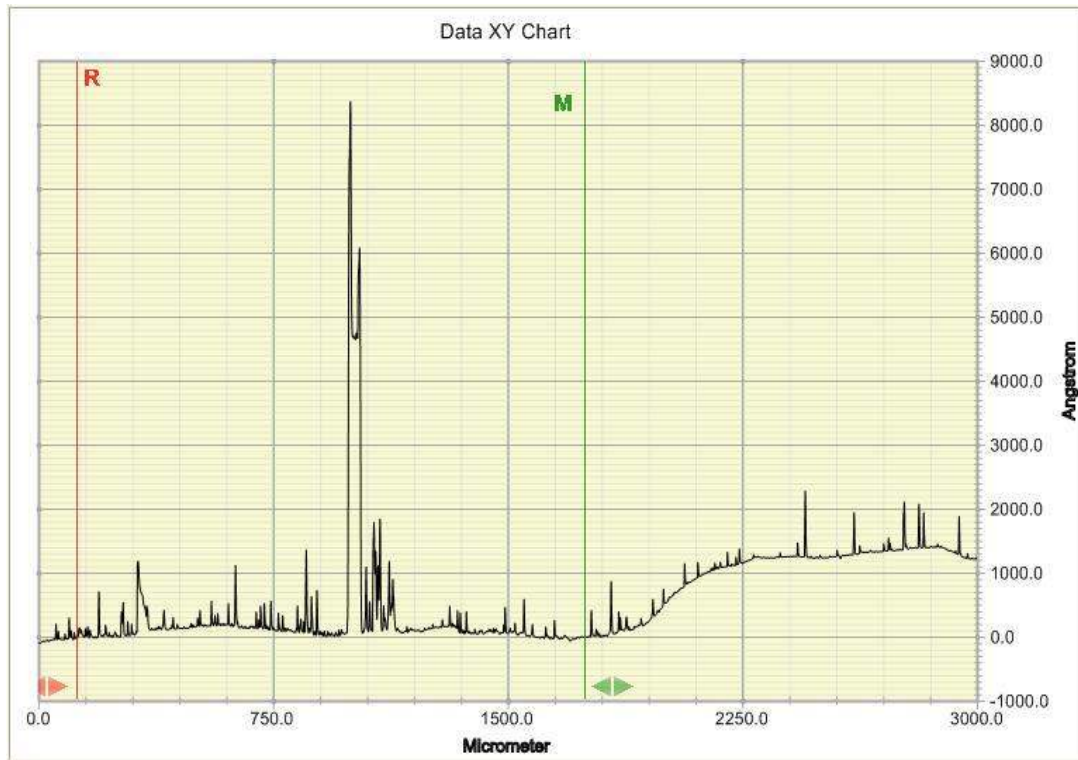


**Fig. 3.7: Surface Profile for ITO on glass showing ITO thickness**

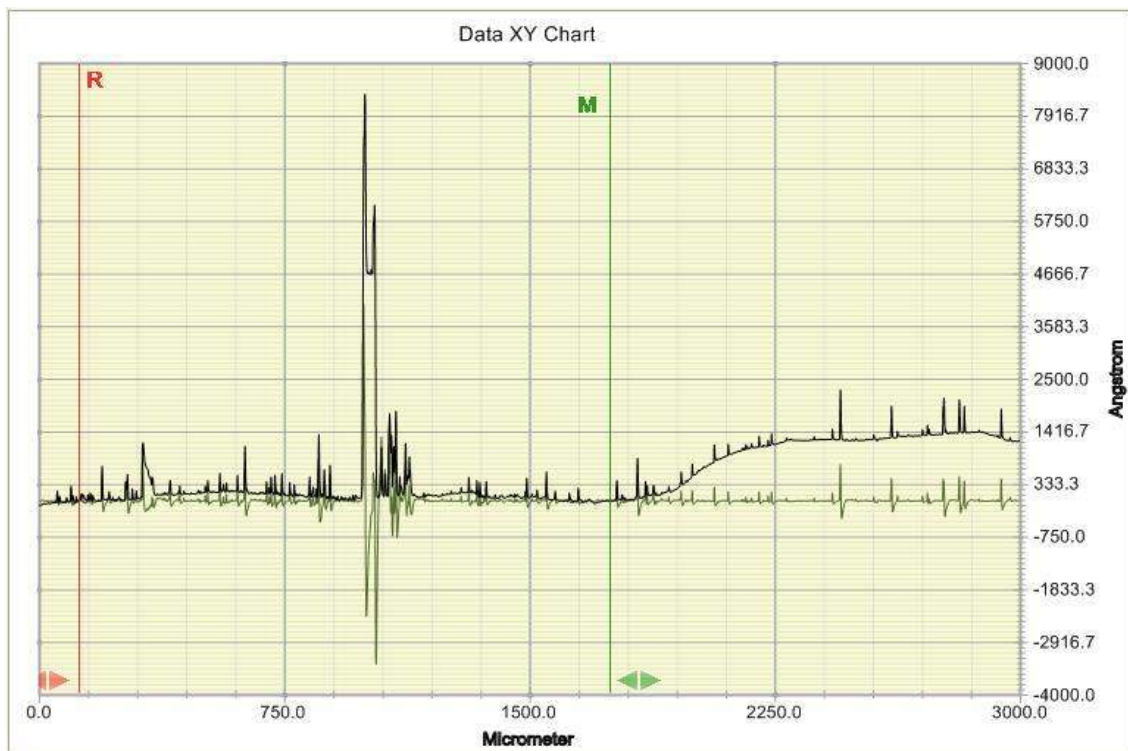


**Fig. 3.8: Surface Profile for ITO on glass showing roughness**

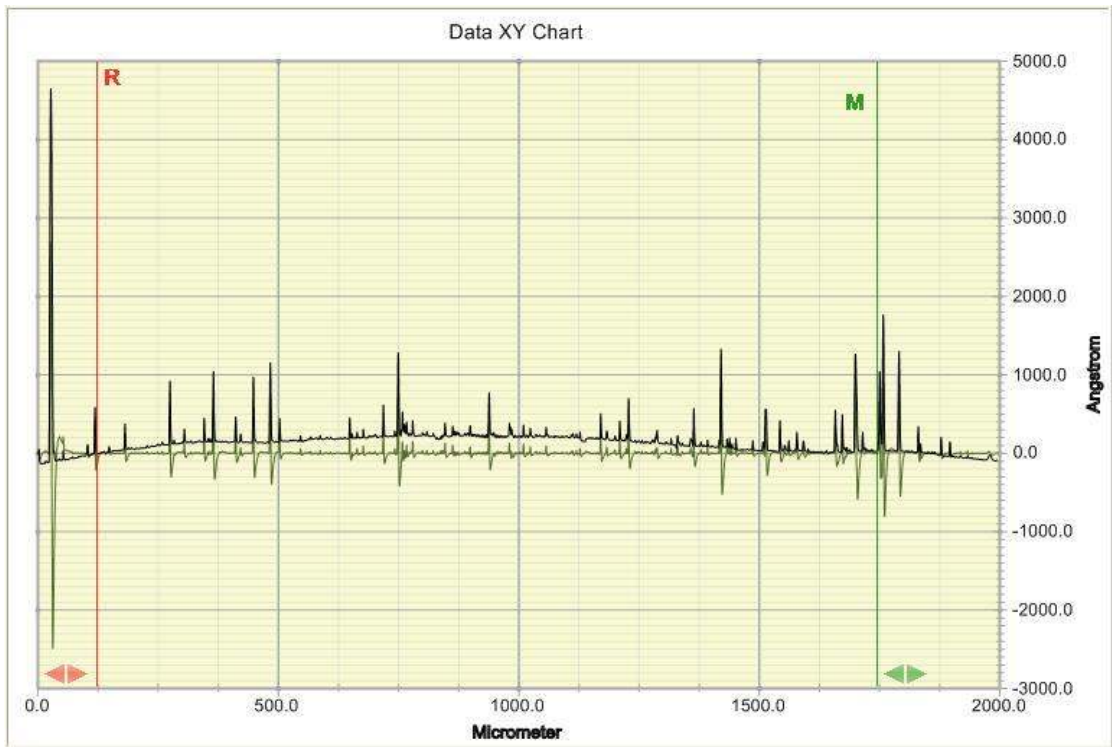


**Fig. 3.9: Surface Profile for PEDOT on glass showing roughness**

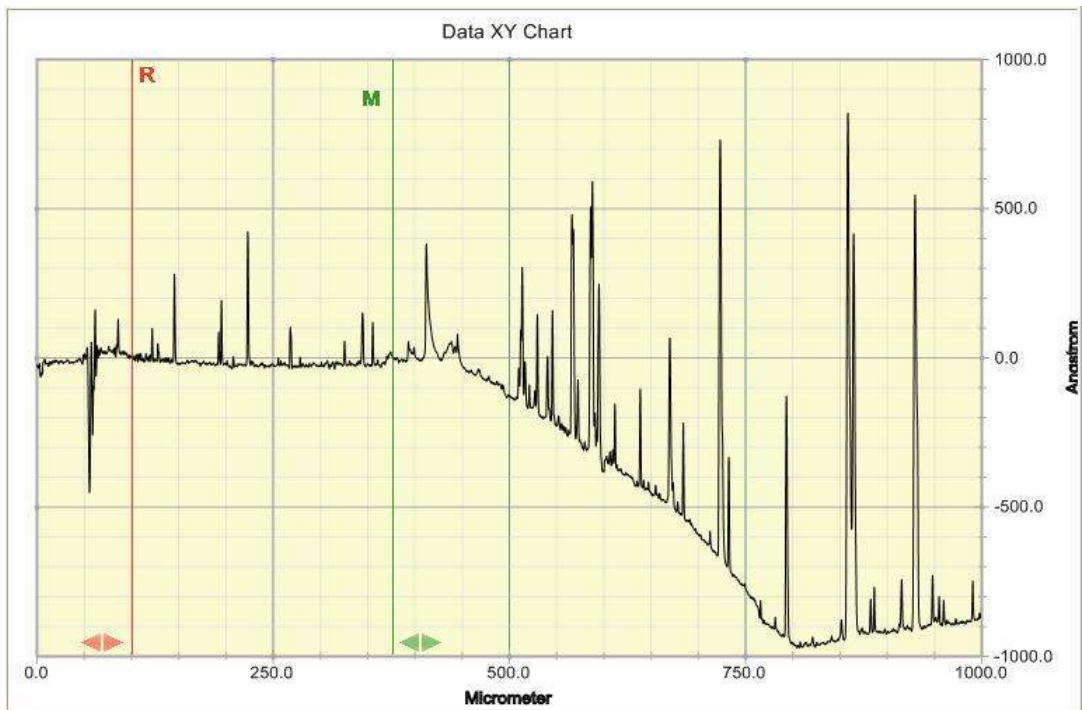


**Fig. 3.10: Surface Profile for PEDOT on ITO showing thickness**

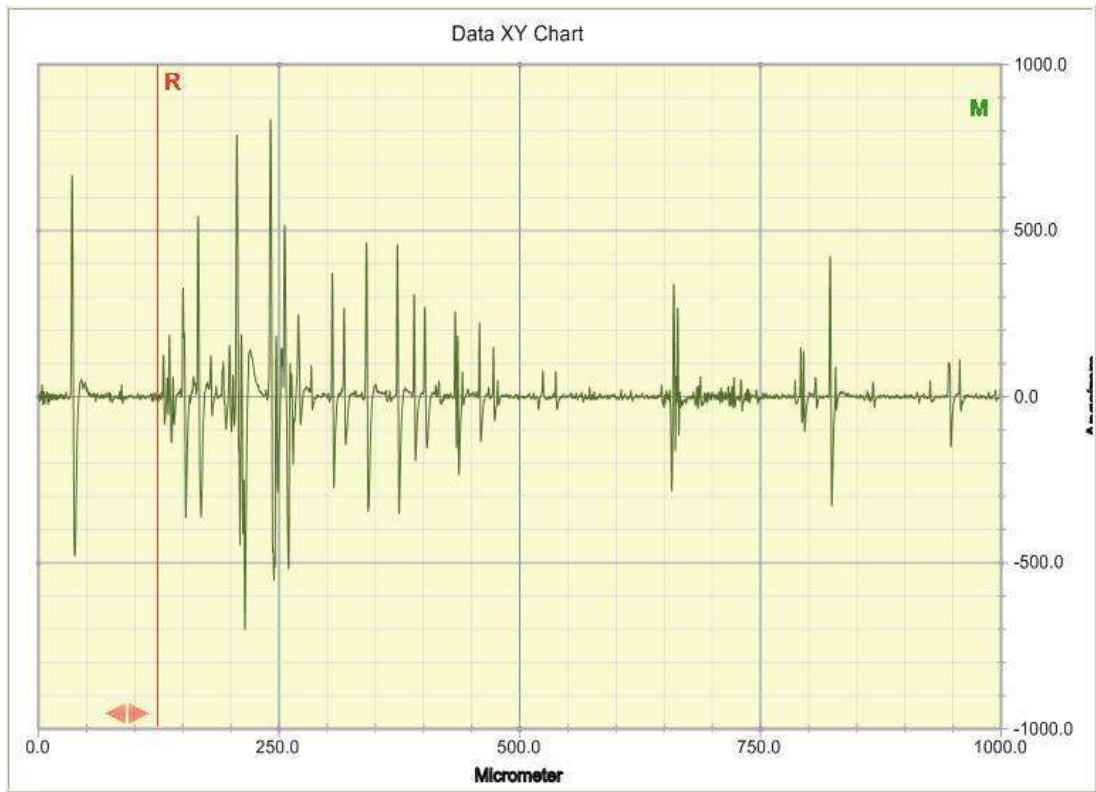


**Fig. 3.11: Surface Profile for PEDOT on ITO showing roughness**

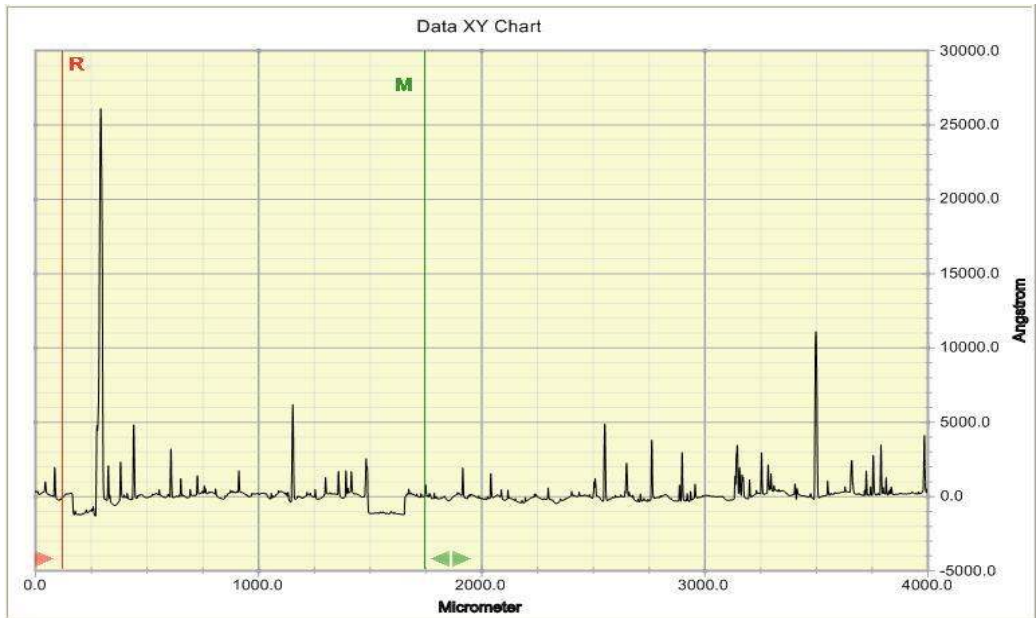


**Fig. 3.12: Surface Profile for MEH-PPV on glass showing thickness**

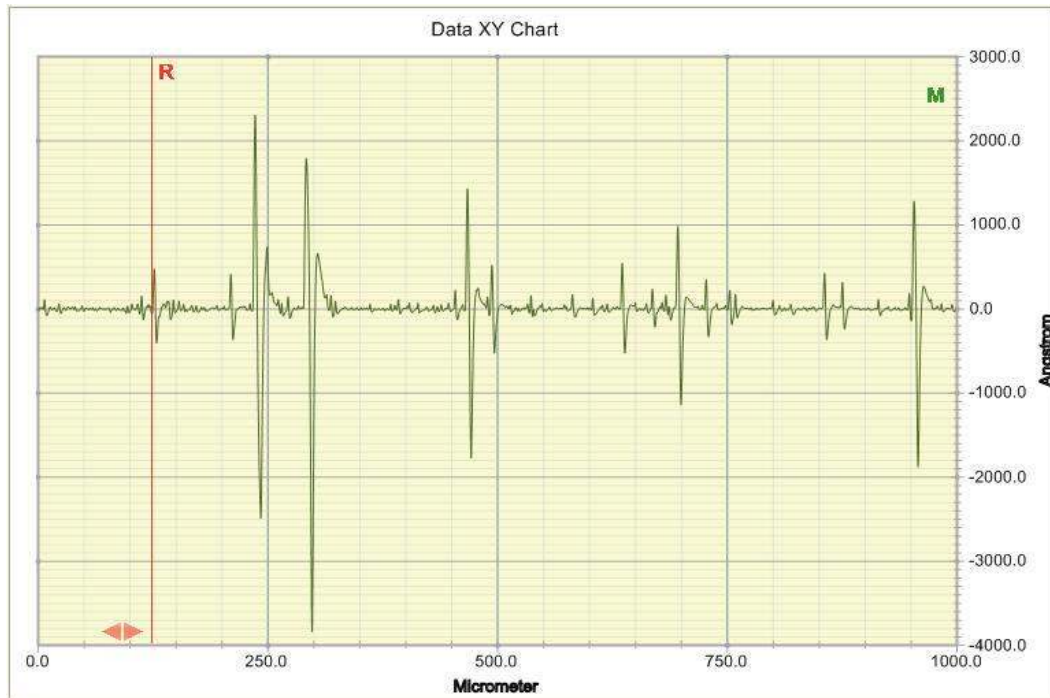


**Fig. 3.13: Surface Profile for MEH-PPV on glass showing roughness**

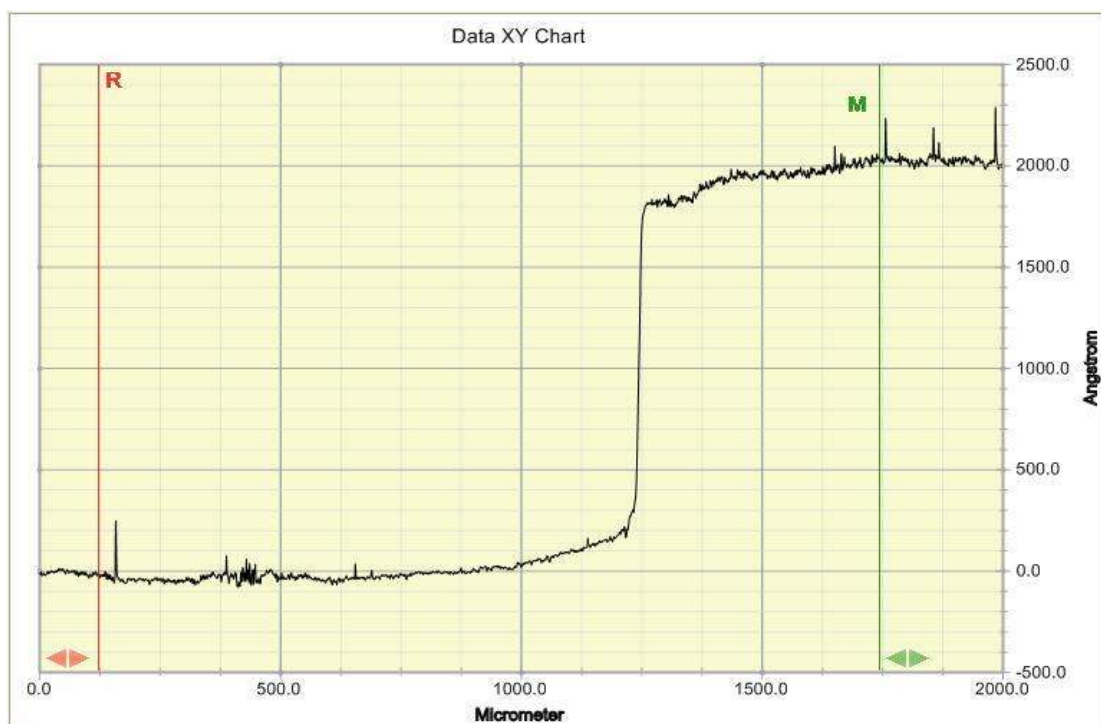


**Fig. 3.14: Surface Profile for Aluminum on glass showing thickness**

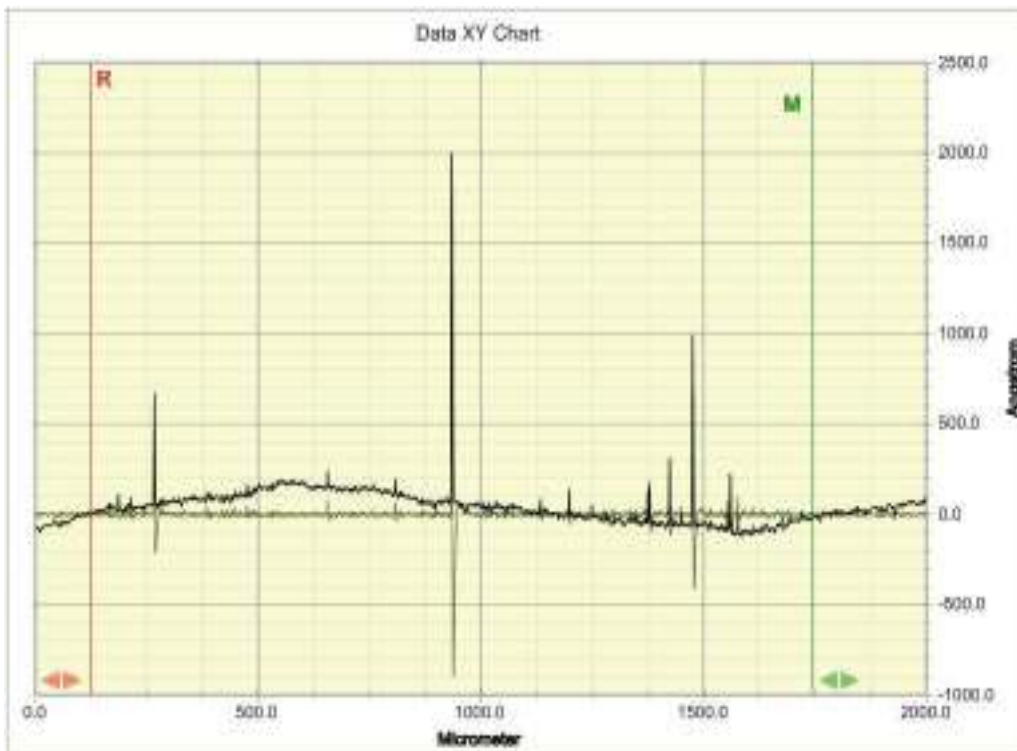


**Fig. 3.15: Surface Profile for Aluminum on glass showing roughness**

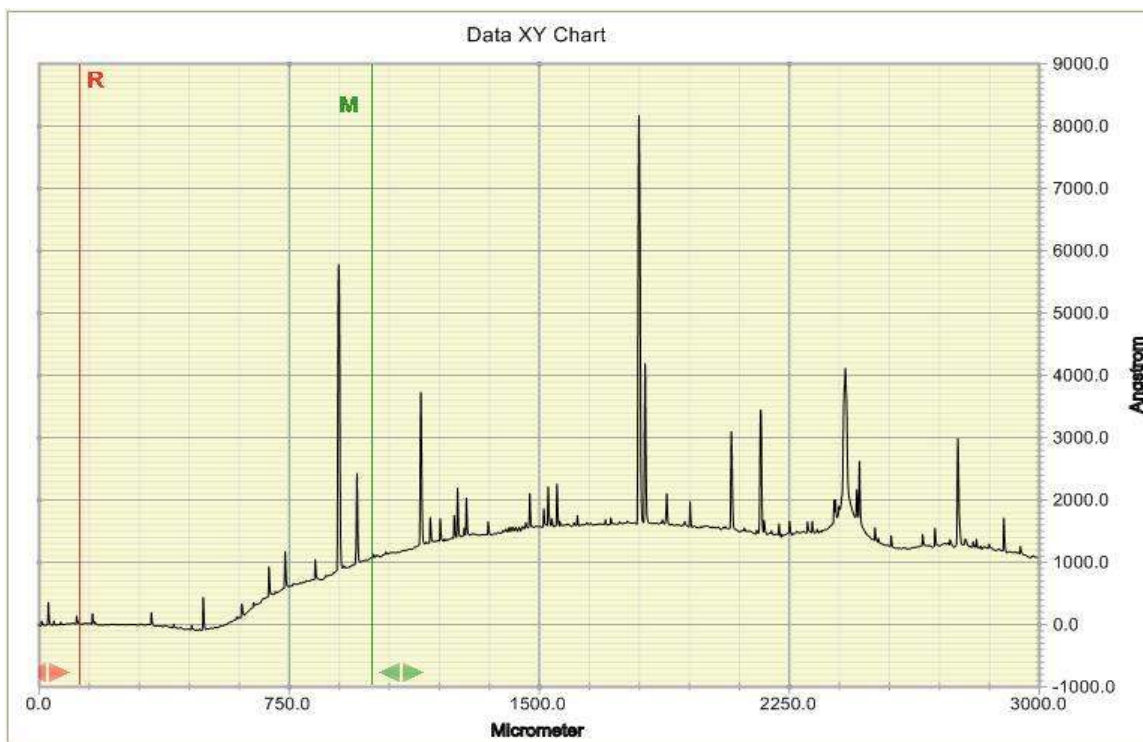


**Fig. 3.16: Surface Profile for PEDOT on ITO showing thickness (heated at 250 °C)**

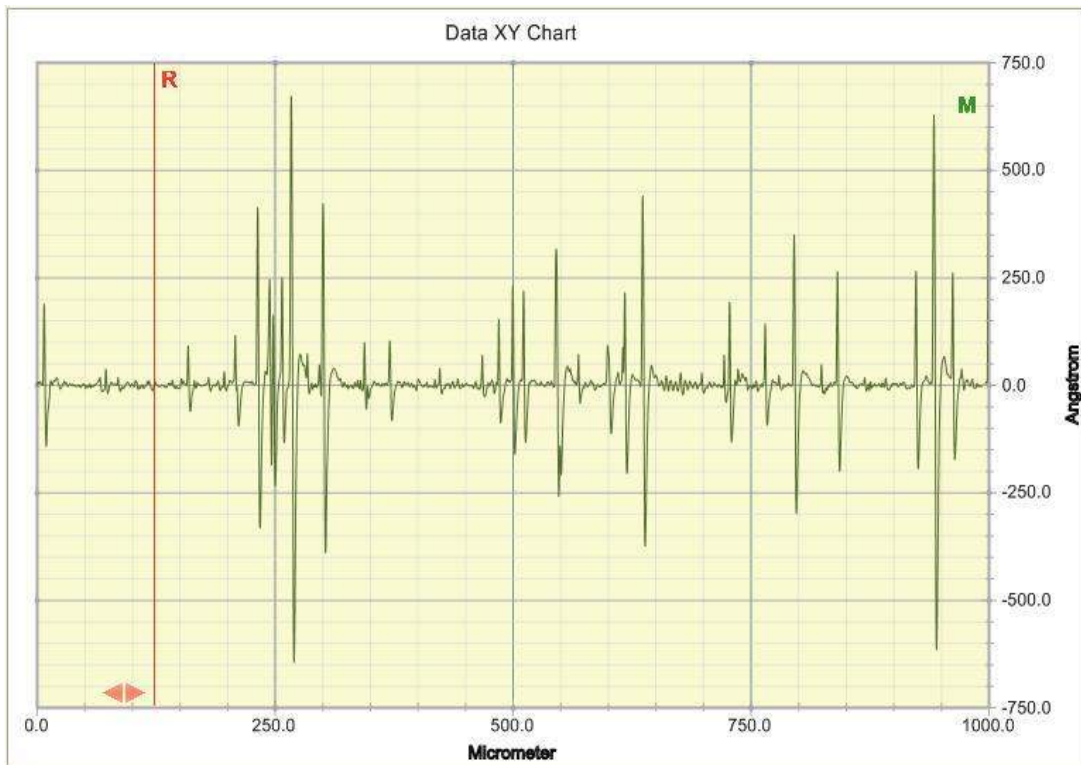


**Fig. 3.17: Surface Profile for PEDOT on ITO showing roughness (heated at 250 °C)**

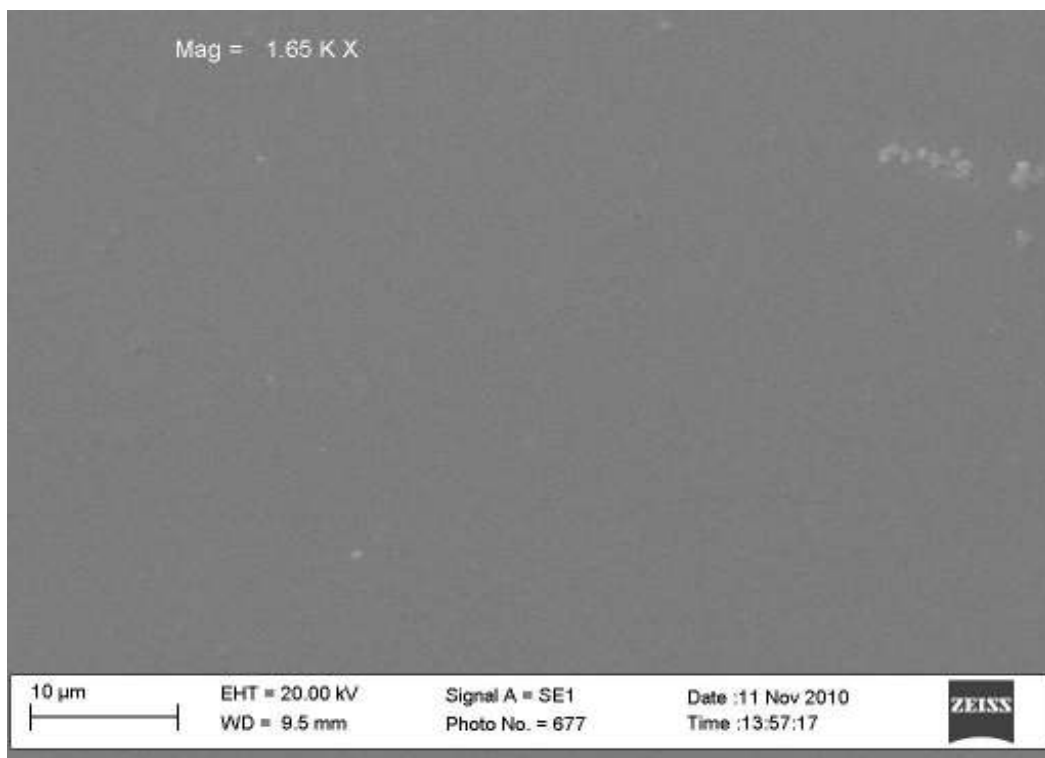


**Fig. 3.18: SEM image for ITO showing surface morphology**

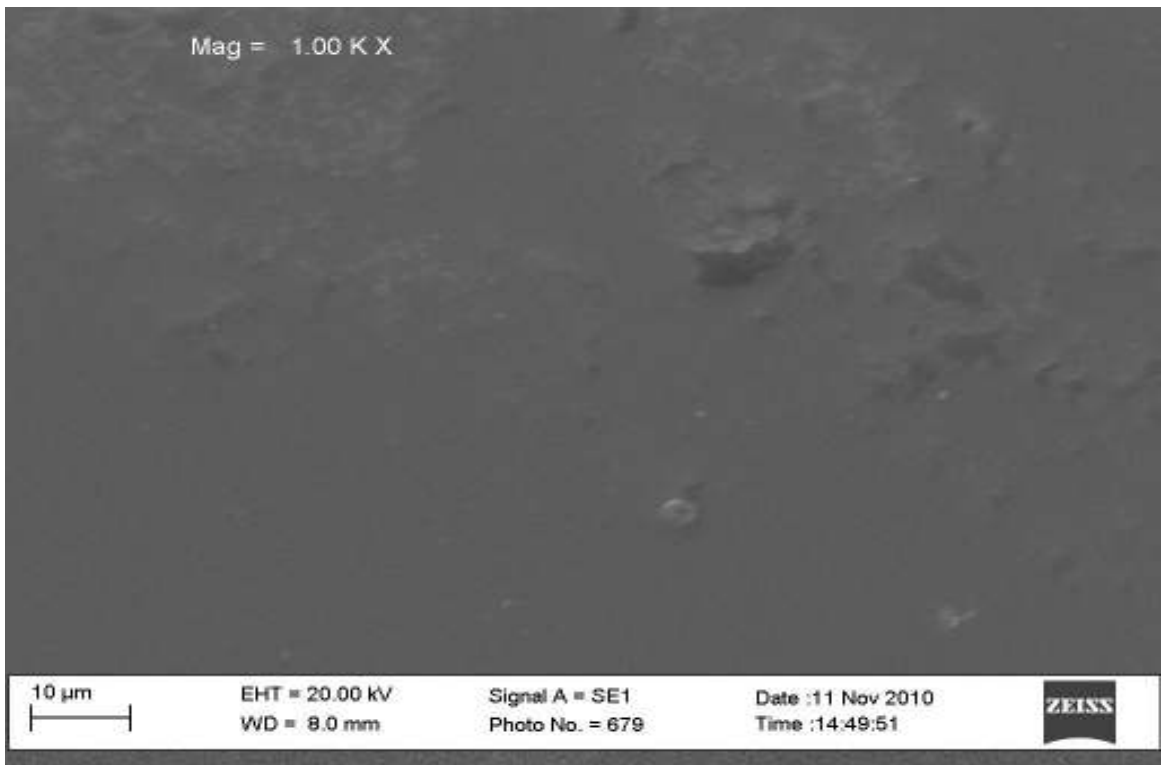


**Fig. 3.19: SEM image for PEDOT:PSS showing surface morphology**

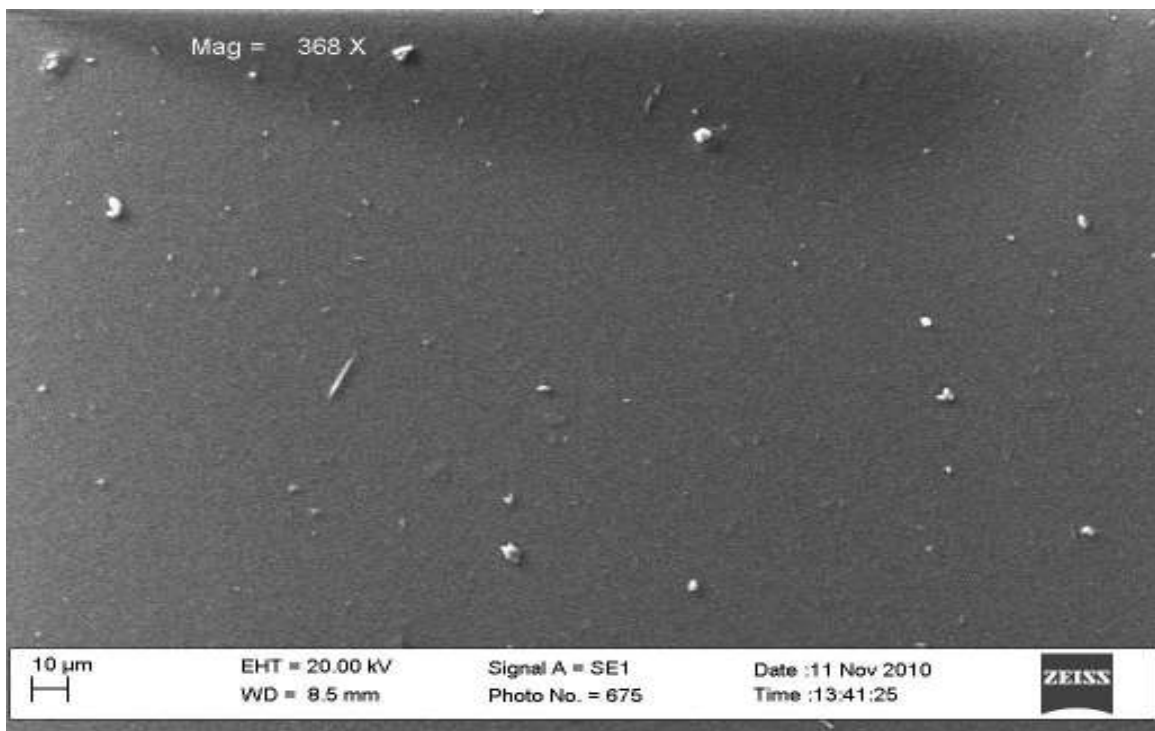


**Fig. 3.20: SEM image for MEH-PPV showing surface morphology**

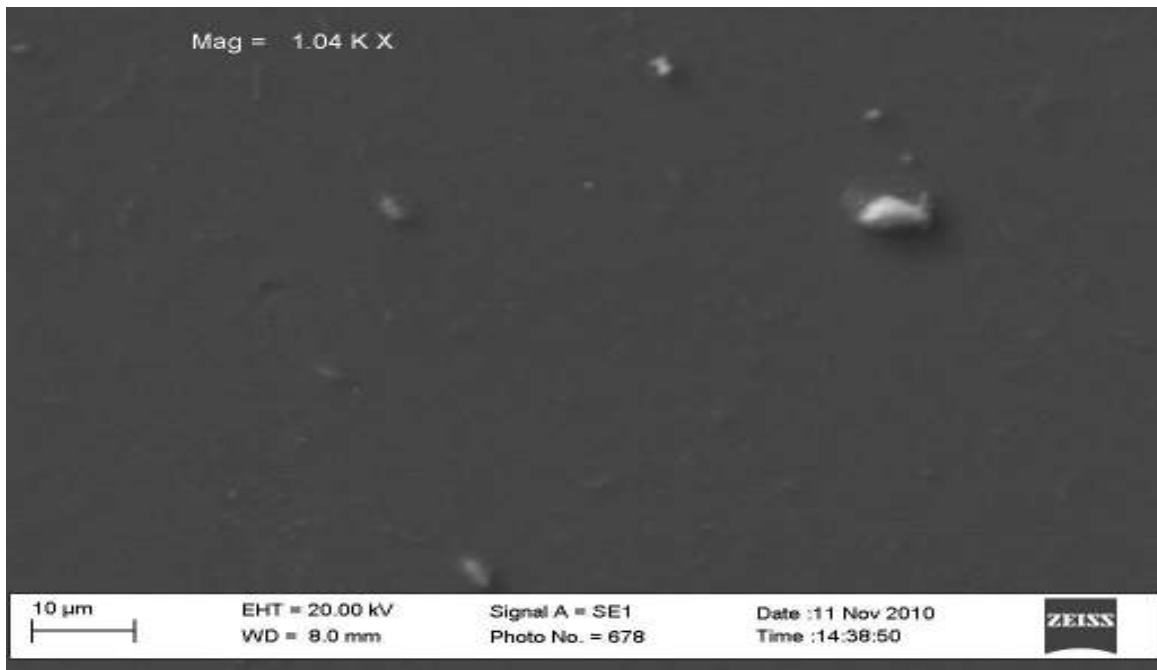


**Fig. 3.21: SEM image for MEH-PPV on ITO showing surface morphology**

The overall layer thicknesses obtained from the surface profilometry measurements are summarized in Table 3.0.

### **3.3.2 Electrical Characterization and Optical Analysis of Thin-Film Layers**

This section mainly describes results of Sheet Resistance from the Four Point Probe system which measures this individual layer characteristic. The Sheet Resistance  $R_s$  is a measure of the resistivity for very thin layers and is represented as shown in Table 3.2 – Table 3.8. All tests were done at room-temperature (RT). The electrical characterization results produced a basis for more efficient devices with lower working voltage and greater emissions when considering more complex multi-layered structures. Sheet resistance values for layers were seen to be dependent on the thickness of deposited thin-films. An increase in thin-film layer, leads to a higher sheet resistance and device turn-on voltage.

A clear distinction is seen when comparing the annealed and unannealed ITO anode layer of

an OLED. Sheet resistance ( $R_s$ ) values reduced by three orders of magnitude (Table 3.2 - Table 3.4). This shows the importance of annealing the ITO layer to improve its electrical properties. The PEDOT:PSS semi-conducting polymer layer also showed relatively high sheet resistance values as compared to ITO and Aluminum metal which showed the least resistance being a metallic cathode layer (Table 3.4 – Table 3.8). MEH-PPV layers had relatively high resistance values and could not be measured using the Four point probe system as the limit to measurements were probably exceeded.

Sample A<sub>I</sub> - ITO layer (Unannealed)

$$R_s = (\pi/\ln 2) * (V/I)$$

Resistance R ( $\Omega$ )	V/I	Thickness ( $\mu\text{m}$ )	Sheet resistance $R_s$ ( $\Omega$ )
2.52E+006	5.53E+005	0.1	2.51E+006
2.25E+006	4.95E+005	0.1	2.24E+006
1.81E+006	3.99E+005	0.1	1.80E+006
2.18E+006	4.81E+005	0.1	2.17E+006
3.04E+006	6.70E+005	0.1	3.04E+006

**Table 3.2: Sheet resistance values at different points for unannealed ITO layer**

SAMPLE A<sub>II</sub> - ITO layer (annealed)

Annealing was done at 250°C in open air

Resistance R ( $\Omega$ )	V/I	Thickness ( $\mu\text{m}$ )	Sheet resistance $R_s$ ( $\Omega$ )
4.23E+003	9.35E+002	0.1	4.23E+003
3.91E+003	8.64E+002	0.1	3.91E+003
3.66E+003	8.09E+002	0.1	3.66E+003
3.85E+003	8.50E+002	0.1	3.85E+003
4.48E+003	9.90E+002	0.1	4.49E+003

**Table 3.3: Sheet resistance values at different points for annealed ITO on glass layer**

Sample A<sub>III</sub> - Annealed ITO layer on glass substrate

Resistance R ( $\Omega$ )	V/I	Thickness ( $\mu\text{m}$ )	Sheet resistance $R_s$ ( $\Omega$ )
4.24E+003	9.37E+002	0.12	4.24E+003
3.68E+003	8.12E+002	0.12	3.68E+003
3.30E+003	7.29E+002	0.12	3.30E+003
4.27E+003	9.44E+002	0.12	4.28E+003
4.02E+003	8.89E+002	0.12	4.03E+003

**Table 3.4: Sheet resistance values at different points for annealed ITO on glass layer**

Sample B<sub>I</sub> - PEDOT:PSS on glass substrate

Resistance R ( $\Omega$ )	V/I	Thickness ( $\mu\text{m}$ )	Sheet resistance $R_s$ ( $\Omega$ )
9.46E+005	2.08E+005	0.07	9.42E+005
8.59E+005	1.89E+005	0.07	8.56E+005
7.69E+005	1.69E+005	0.07	7.65E+005
1.08E+006	2.39E+005	0.07	1.08E+005
6.95E+005	1.54E+005	0.07	6.97E+005

**Table 3.5: Sheet resistance values at different points on a PEDOT:PSS layer**

Sample B<sub>II</sub> - PEDOT:PSS on glass

Resistance R ( $\Omega$ )	V/I	Thickness ( $\mu\text{m}$ )	Sheet resistance $R_s$ ( $\Omega$ )
1.08E+006	2.39E+005	0.05	1.08E+006
5.91E+005	1.30E+005	0.05	5.88E+005
6.27E+005	1.38E+005	0.05	6.25E+005
6.16E+005	1.36E+005	0.05	6.16E+005
1.37E+005	3.03E+005	0.05	1.37E+005

**Table 3.6: Sheet resistance values at different points on a PEDOT:PSS layer**

Sample C<sub>1</sub> – PEDOT:PSS on ITO

Resistance R (Ω)	V/I	Thickness (μm)	Sheet resistance R <sub>s</sub> (Ω)
1.30E+003	2.87E+002	0.1	1.29E+003
1.67E+003	3.70E+002	0.1	1.68E+003
1.67E+003	3.70E+002	0.1	1.67E+003

**Table 3.7: Sheet resistance values at different points for a layer of PEDOT:PSS on ITO**

Sample F – Aluminum on glass layer

Resistance R (Ω)	V/I	Thickness (μm)	Sheet resistance R <sub>s</sub> (Ω)
2.30E-001	5.08E-002	0.15	2.30E-001
2.86E-001	6.32E-002	0.15	2.80E-001
2.25E-001	4.96E-002	0.15	2.20E-001
2.37E-001	5.23E-002	0.15	2.30E-001
2.46E-001	5.42E-002	0.15	2.40E-001

**Table 3.8: Sheet resistance values at different points for Aluminum layer on glass**

### 3.3.3. Optical Characterization of Thin-Film layers

This section describes the Spectral properties of the different layers making up the OLED mainly considering the Transmittance T. When light travels through a thin film layer, it is either absorbed, reflected or transmitted. Absorbance, Reflectance, and Transmittance are optical properties which can be analysed from the spectrum produced during the process of light travel. A simple equation which relates these three properties is given by:

$$\mathbf{I = T + R + A} \quad (32)$$

in terms of percentage,  $100 = T + R + A$

where T is a measure of the Transmittance, R is the Reflectance and A is the Absorbance.

For a good OLED, we wish to increase the transmittance of the ITO layer and reduce the absorbance and reflectance. (Fig. 3.22 – Fig. 3.28) gives the results obtained for different layers using the spectrophotometer to analyse the transmittance spectrum.

A transmittance of 100% was obtained with air between the slits and detector on the optical fibre. However on inserting a glass slide, transmittance T reduced to about 90% (Fig. 3.22).

At wavelengths less than 300 nm, there is no transmittance through the glass slide. For ITO thin-film layer on glass, it was observed that annealing also improved its optical characteristic by increasing the transmittance to about 95% at wavelengths of 400 - 450 nm range as compared to an 85% transmittance value for the unannealed ITO at the same wavelength range (Figs. 3.23 & 3.24). The transmittance of PEDOT:PSS layer on glass showed better results for a wide range of wavelength values when compared with that spin coated on ITO. The relatively high transmittance was reduced by about 10% at wavelength of about 450 – 600 nm and is suspected to be due to the combined effect with the underlying ITO layer (Figs. 3.25 & 3.26). For the MEH-PPV layer, a transmittance value of about 52% at a wavelength of 510 nm was obtained (Figs. 3.27 & 3.28). Similar transmittance spectra was observed for the hybrid MEH-PPV+TiO<sub>2</sub> layer which means that incorporating TiO<sub>2</sub> nano particles did not affect the transmission spectra of the polymer organic layer.

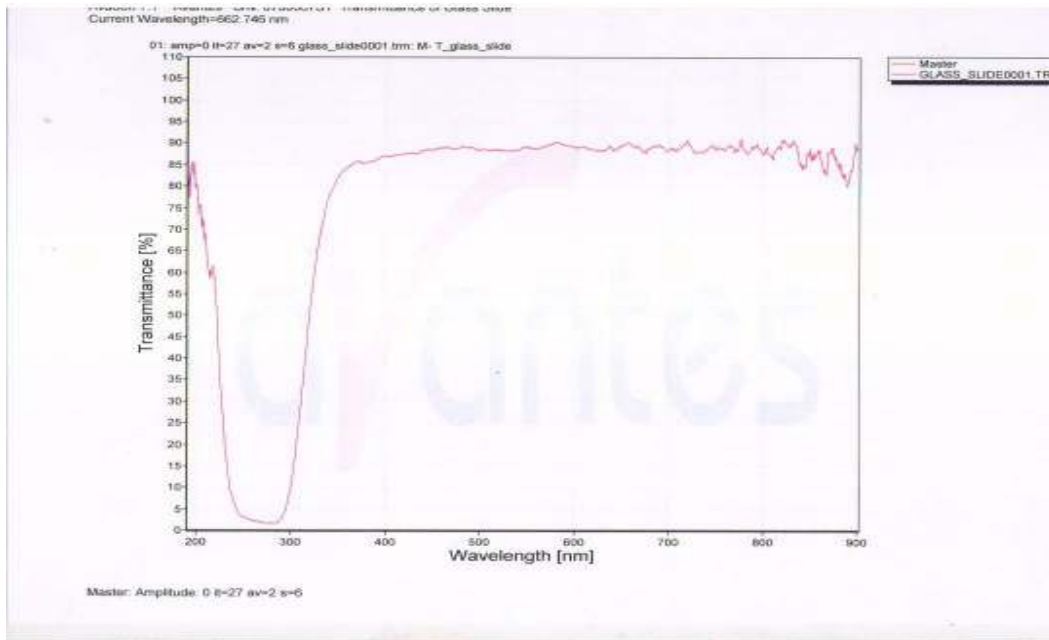


**Fig. 3.22: Transmittance spectra of a plane glass slide**

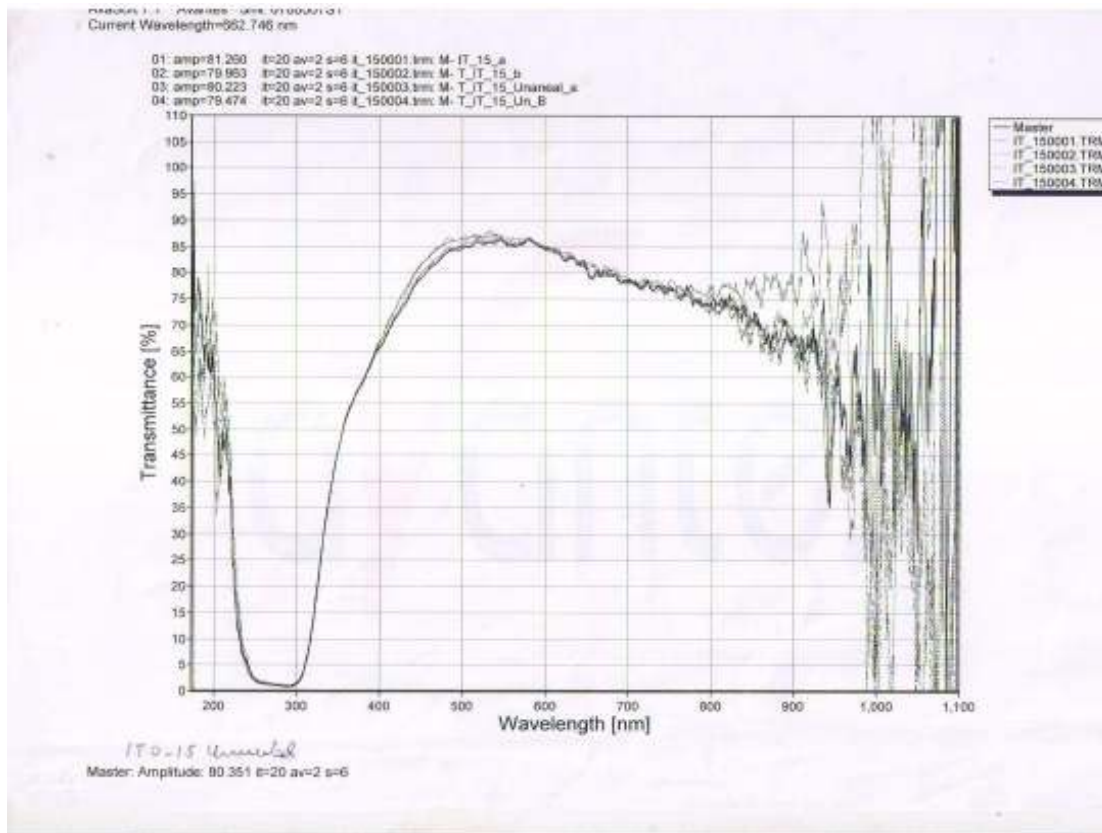


**Fig. 3.23: Transmittance spectra of ITO on glass substrate (unannealed)**

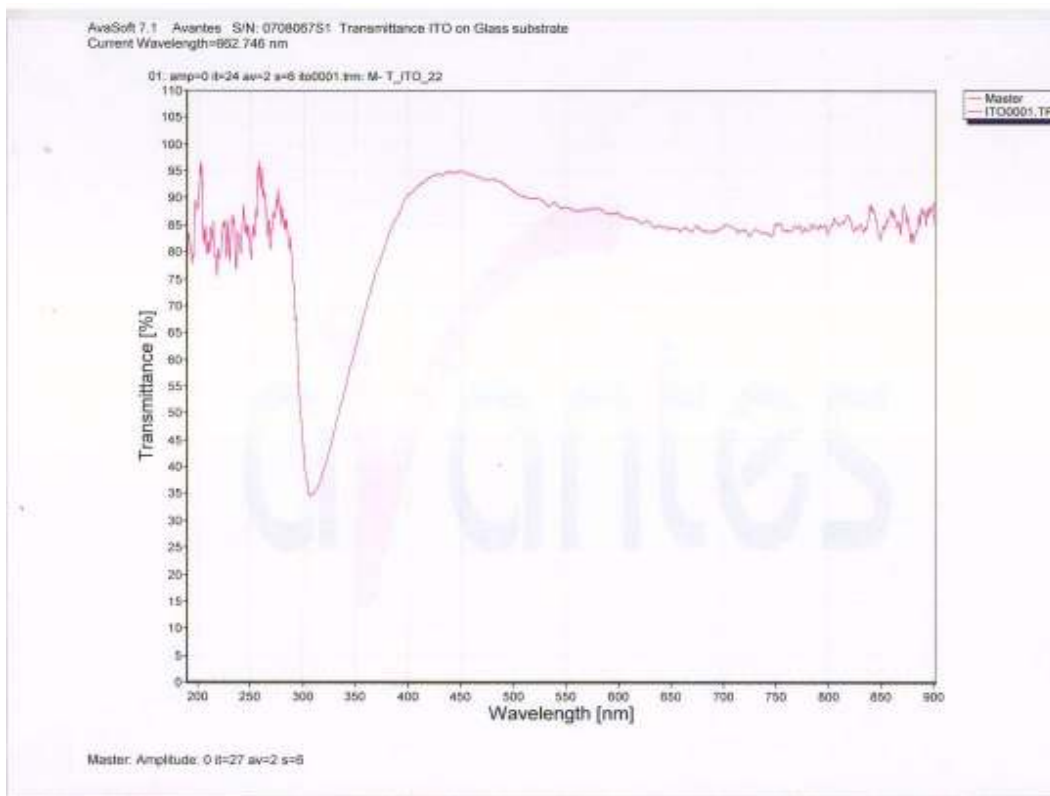


**Fig. 3.24: Transmittance spectra of ITO on glass substrate (annealed)**

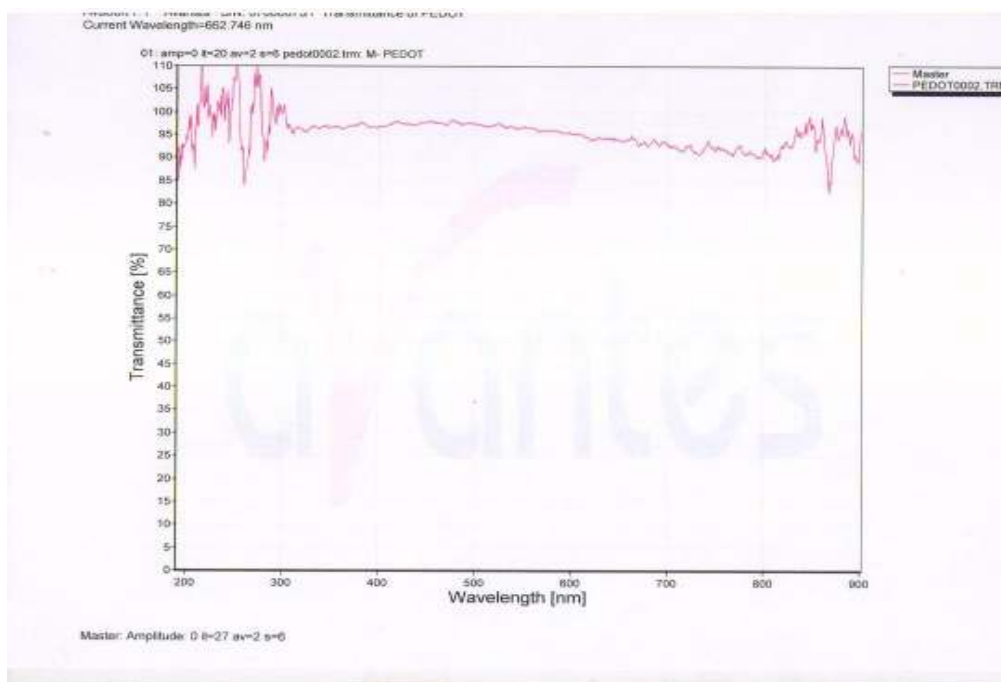


**Fig. 3.25: Transmittance spectra of PEDOT:PSS on glass substrate (air as reference)**



**Fig. 3.26: Transmittance spectra of PEDOT:PSS on ITO**



**Fig. 3.27: Transmittance spectra of MEH-PPV on glass**

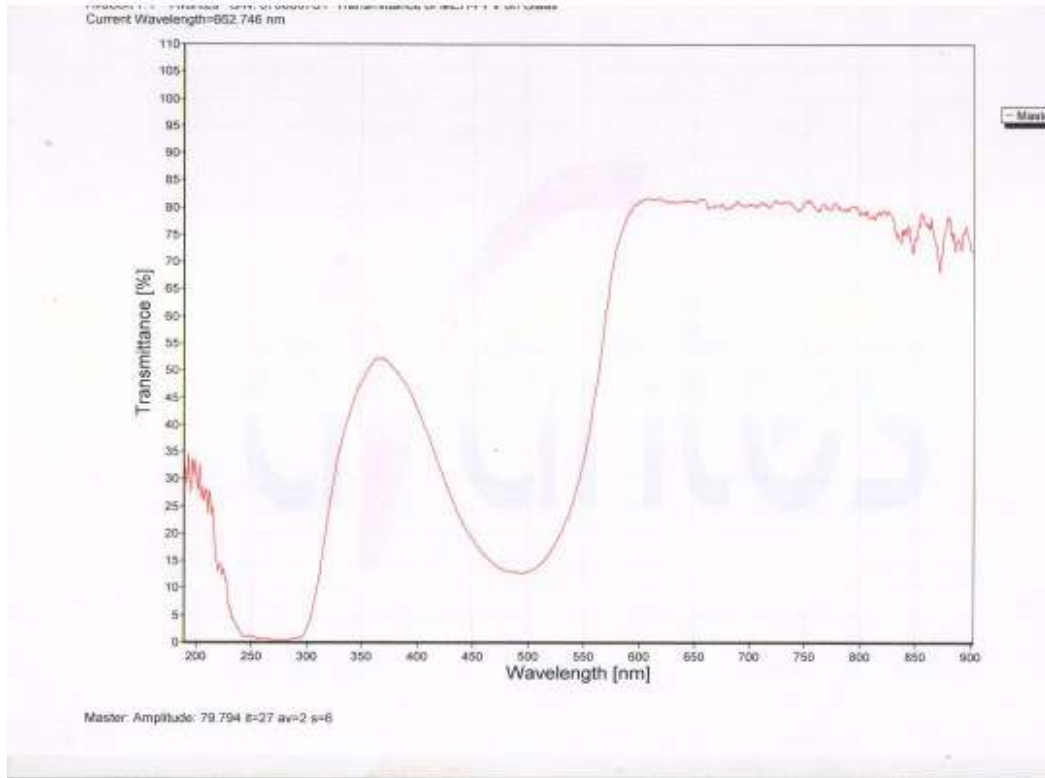


**Fig. 3.28: Transmittance spectra of MEH-PPV+TiO<sub>2</sub> on glass**

### 3.3.4 I-V Characterization and Spectral Analysis of light emitted from device

This section describes the working device properties in terms of current and voltage measured using the Keithley DC Source Meter. A specified forward bias current was applied in the sweep mode with a corresponding working turn-on voltage  $V_o$  being measured from the I-V data values obtained. For a normal working OLED, there is a limiting voltage called the **turn-on voltage** after which further increase in current leads to little or no significant voltage change. This is the point in which the device emits its characteristic yellowish-orange light. The intensity of the emitted light was measured and analysed using a light sensitive optical fibre detector of the spectrophotometer. Fig. 3.29 shows the general nature of the I-V curve for a working HOILED with a forward bias current applied and the turn on voltage is about 10V. The corresponding I-V curve for the OLED is shown in Fig. 3.30.

The turn on voltage is less in the hybrid device than in the normal OLED as shown in the figures. Efficiency of devices also depends on the current – voltage characteristics and the mode of charge transport. A device with minimal voltage across with sufficient current flowing through it produces an efficient and stable device. The J-V curves for the OLED are presented in Figs. 3.31 and 3.32 where measurements are taken for current density ( $A/cm^2$ ) versus voltage (volts). The area of the active region of the device also determines the amount of current required to emit light from the device. Smaller areas will require less turn-on voltages to operate them. The J-V plots gave much linear shaped curves with some peculiarities at high voltage. The shape of the curve may be attributed to the mode of charge transport, which is, actively tunneling of charges across barriers.

In Fig. 3.33, an excess forward bias current of 40mA lead to the device getting damaged at about a voltage of 80V after emitting light for a few seconds before burning out. Further I-V measurements carried out at later times reveal a degrading trend in electrical properties. All measurements were performed in normal room conditions and rapid increase in turn-on voltage took place after a bias was applied across the device. The device I-V measurements at different time intervals are shown in Figs. 3.34 - 3.36.

**Fig. 3.29: I-V Characteristic curve for a HOILED with forward bias current**

**Fig. 3.30: Typical I-V Characteristic curve for an OLED with forward bias current**

**Fig. 3.31: J-V Characteristic curve for an OLED with forward bias current**

**Fig. 3.32: J-V Characteristic curve for an OLED with forward bias current**

**Fig. 3.33: I-V Curve for OLED with excess applied forward bias**

**Fig. 3.34: I-V Characteristic curve for an OLED with forward bias current at 10 mins**

**Fig. 3.35: I-V Characteristic curve for an OLED with forward bias current at 25 mins**

---

**Fig. 3.36: I-V Characteristic curve for an OLED with forward bias current at 45 mins**

### **3.3.5 Spectral Analysis of light emitted from device**

This section describes the characteristics of emitted light produced when a bias current is applied to the device. The nature of the peaks at different wavelengths is also analysed.

#### **3.3.5.1 Device Spectral Analysis**

As described earlier in Section 3.3.4, the emitted light was optically characterized using a photo-detector of the spectrophotometer by probing with an optical fibre. This gave a spectrum with distinct peaks at wavelengths of the range of 550 – 600nm. This wavelength range falls within the visible region of the electromagnetic spectrum and as such explains the reason why we see the characteristic emitted light. Figs. 3.37-3.39 shows the plots magnified to a high resolution, as such noise peaks are seen unfiltered.

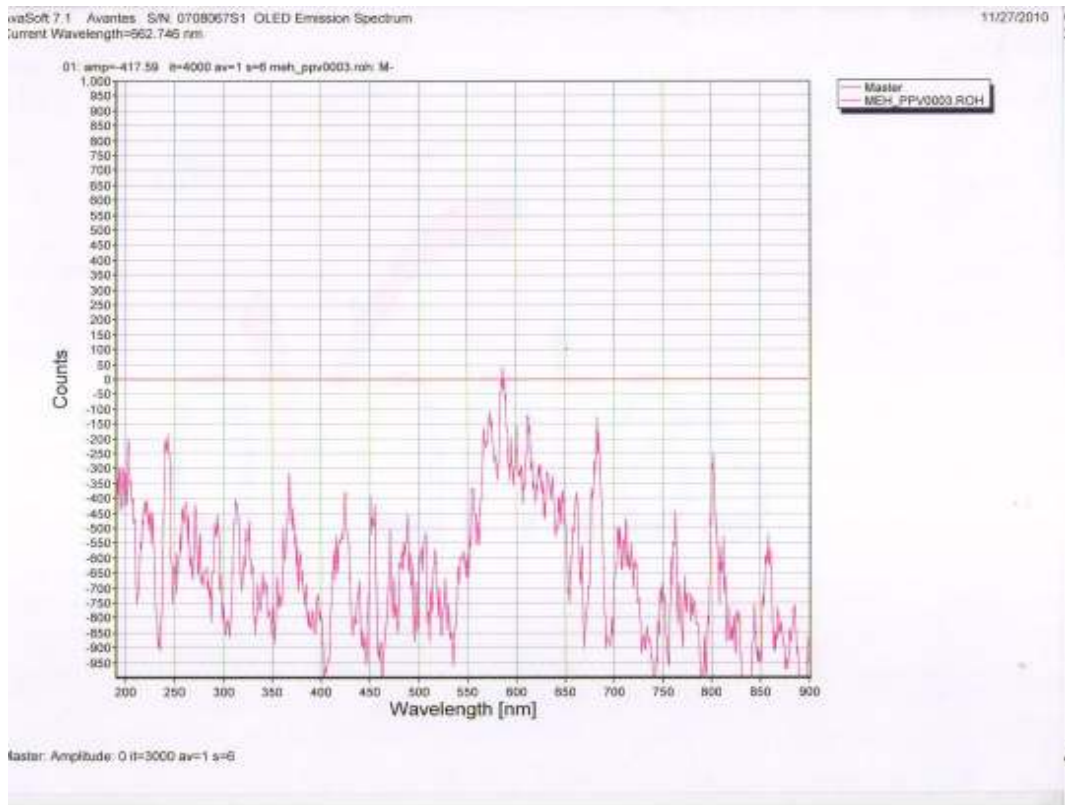


**Fig. 3.37: Spectrum of light emitted (from high magnification showing noise on background)**

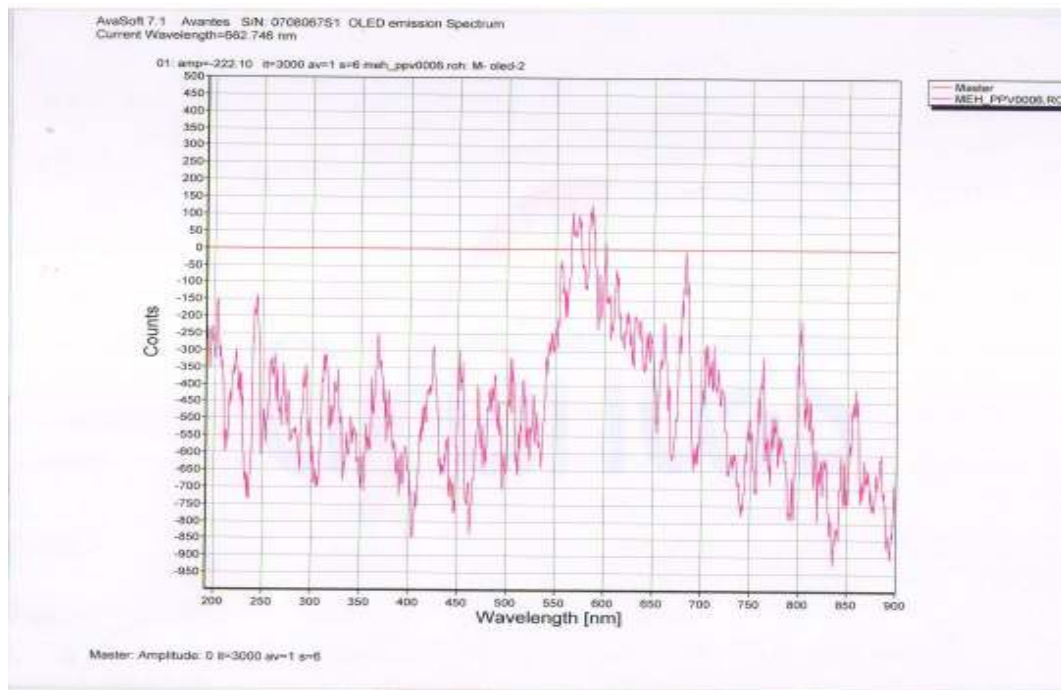


**Fig. 3.38: Spectrum of light emitted (from high magnification showing noise on background)**

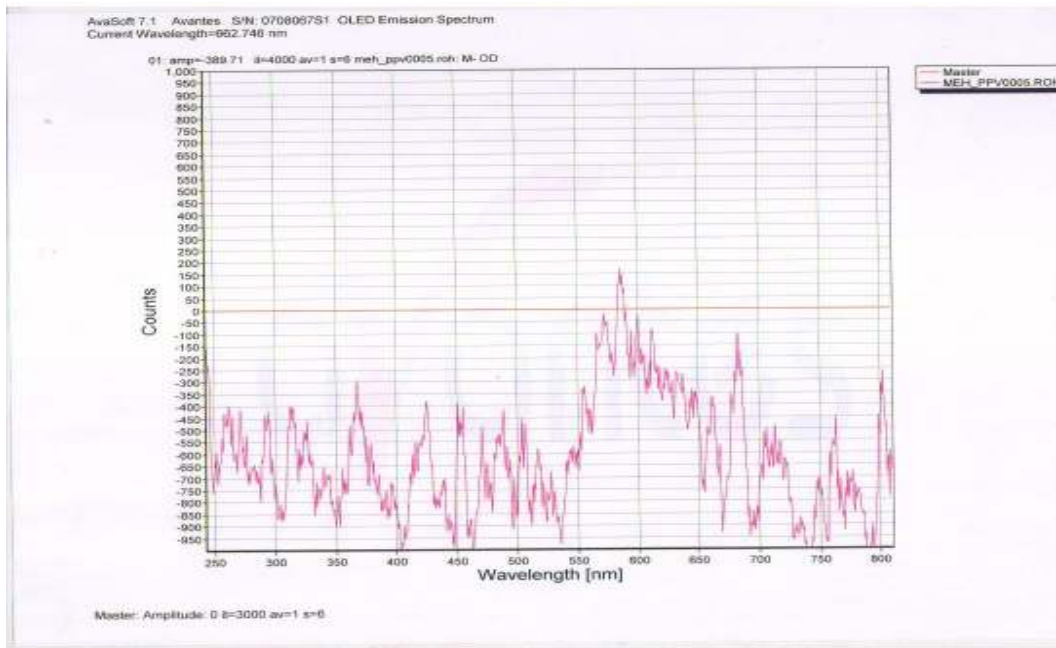


**Fig. 3.39: Spectrum of light emitted (from high magnification with noise unfiltered)**

### 3.3.6 Adhesion Measurements

This section presents the results from adhesion analysis carried out on the different individual layers that make up an OLED/HOILED. Adhesion results were obtained through a collaborative work carried out with Tiffany Tong at Princeton University. Some of her results from earlier publications were also incorporated into this study with prior permission. These include results of average forces and adhesion energies between organic-organic MEH-PPV/ PEDOT:PSS and organic-inorganic PEDOT:PSS/ITO layers.<sup>[46]</sup> AFM results can be used for the ranking of adhesion between different surface pairs relevant to device electronic structure. This is also important in selecting materials for possible device applications like lamination and cold-welding in which device parts are separately fabricated and components assembled with pressure. Strongly adhering interfaces are thus good candidates for contact layers.

The pairwise interactions between these layers is expressed in terms of the average pull-off

forces,  $F_{\text{pull}}$  and adhesion energies,  $G$ . There exists a wide range of adhesive forces exhibited between the surface pair interactions as shown in Fig. 3.40 and summarized in Table 3.9. The highest average pull-off force exists between organic-organic PEDOT:PSS/MEH-PPV layers. A relatively high average pull-off force is also exhibited by the (MEH-PPV+TiO<sub>2</sub>)/Glass substrate; however it is not as high when compared with the same hybrid polymer on a PEDOT:PSS underlying layer.

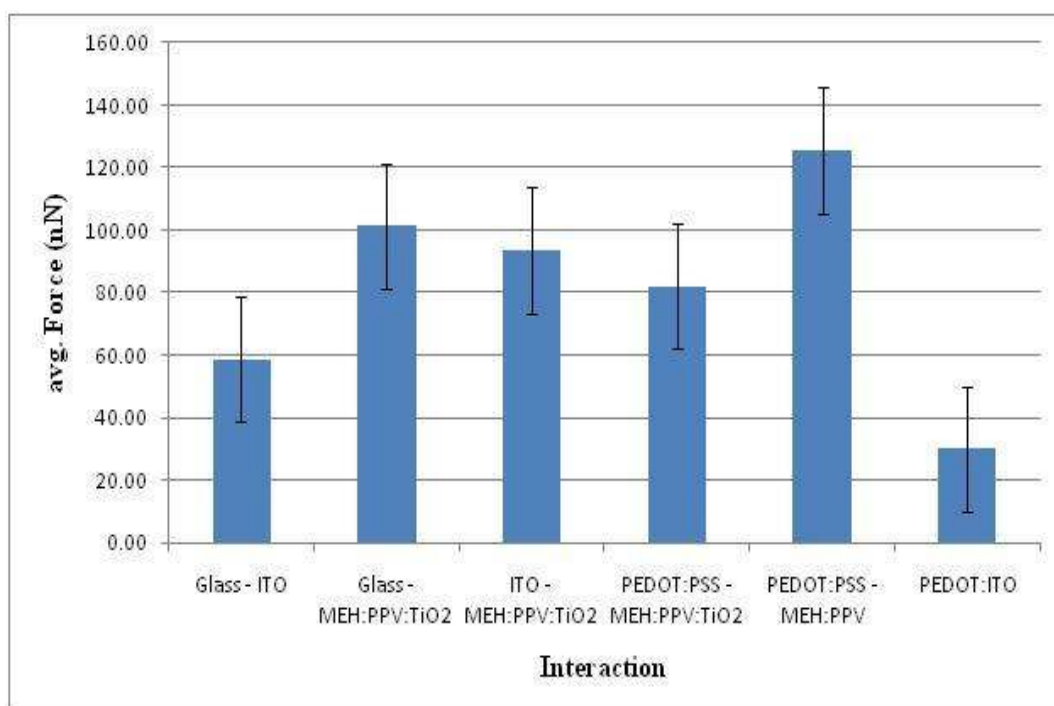


**Fig. 3.40: Average adhesion forces obtained for OLED/HOLED layer structures**

The plots of adhesion energies gives a clearer understanding to the adhesion results obtained and shows more clearly the variance among these layers (Table 3.10). Further studies were carried out on the layers of a hybrid structure with TiO<sub>2</sub> nano particles and very interesting results were obtained for the numerous layers. This is also presented in Figs. 3.40 & 3.41.

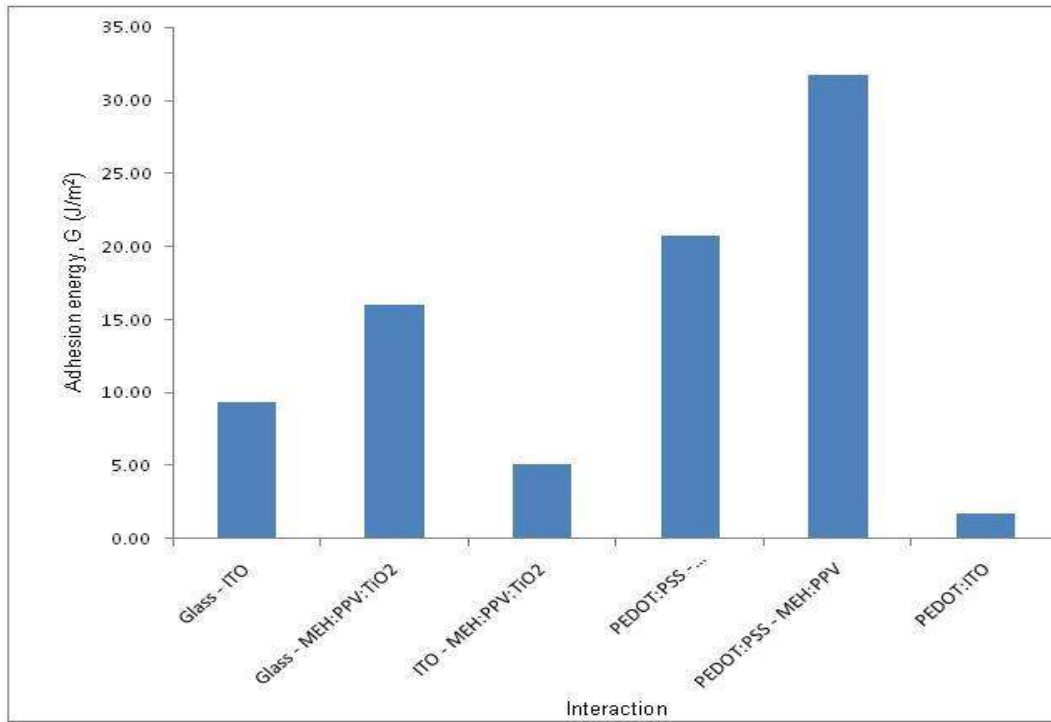


**Fig. 3.41: Average adhesion energies obtained for OLED/HOILED layer structures**

For the adhesion energy, PEDOT:PSS/MEH-PPV still dominated the set of layers under analysis and the lowest was organic-inorganic PEDOT:PSS/ITO layers with an average energy of about  $1.7 \text{ J/m}^2$ . Next to the least were ITO/MEH-PPV+TiO<sub>2</sub> and this shows that the adhesive property of the ITO layer is generally poor with respect to other layers of the device.

Tip coat	Substrate coat	Spring constant (N/m)	Average force (nN)	Standard deviation
MEH-PPV:TiO <sub>2</sub>	PEDOT:PSS	0.56	81.93	23.23
MEH-PPV:TiO <sub>2</sub>	Glass	0.56	101.3	26.58
MEH-PPV:TiO <sub>2</sub>	ITO	0.56	93.54	28.72
ITO	Glass	0.87	58.24	14.53
*ITO	PEDOT:PSS	-	30	6.7
*PEDOT:PSS	MEH-PPV	-	126	28

**Table 3.9: Average adhesion force data for various pairwise interactions of OLED and**

**HOILED layers**

From the results presented in the tables, we see that adhesion cannot be attributed to the improvements observed in device I-V characteristics.

Tip coat	Substrate coat	Substrate Roughness (nm)	Tip radius	Average energy (J/m <sup>2</sup> )
MEH-PPV:TiO <sub>2</sub>	PEDOT:PSS	0.63	250	20.75
MEH-PPV:TiO <sub>2</sub>	Glass	1.01	250	16.03
MEH-PPV:TiO <sub>2</sub>	ITO	2.94	250	5.15
ITO	Glass	1.01	166.67	9.31
*ITO	PEDOT:PSS	-	-	1.7
*PEDOT:PSS	MEH-PPV	-	-	32

**Table 3.10: Average adhesion energies for various pairwise interactions of OLED and HOILED layers**

(Note - interactions in Tables. 3.9 & 3.10 with asterisk \* are results incorporated from collaborative earlier work of Tong et al.)

### 3.3.7 Implications

The implications of the general characterization results obtained for both device and layer configuration are quite significant in understanding the normal operation of an OLED or HOILED.

Initially, the roughness results for different layers which make up the device enables a better selection of material combination in devices where a wide range of materials is being considered for different applications. These applications may include fabricating better light emitting and environmental resistant devices.

The Electrical and Optical Characterization results also produce a basis for more efficient emission of light through the different layers when considering a more complex multi-

layered structure. Sheet resistance values for different layers analysed gives an insight to better current and voltage properties within these layers with required thickness.

AFM results were obtained by adopting earlier models<sup>[46]</sup> which employs an effective radius that combines the effects of both the AFM tip radius and an averaged root mean square surface roughness. However, improvements can be made to calculate local surface roughness values and variations in surface energy across individual layers. Adhesion energy measurements as earlier discussed can be used in Mode I fracture mechanics to estimate interface robustness. They also provide a basis for estimating critical stresses in rigid structures fabricated in this thesis. Pairwise interactions with low adhesion energies are affected by partial debonding during charge transport across interfaces.

The relatively high current densities in regions of partial contact may also lead to localized heating and oxidation of layers which leads to observed degradation in device characteristics observed during device characterization.<sup>[46]</sup>

## CHAPTER FOUR

### 4.0 Summary and Suggestions for Future Work

In order to investigate basic working mechanism of OLEDs and HOILEDs, model devices were fabricated and generally characterized. Normal routine fabrication procedures which include R.F Magnetron Sputtering of Indium Tin-Oxide on glass, thermal annealing of samples to remove sputter-induced damages and reduce sheet resistance, Spin Coating of Organic PEDOT:PSS layer to smoothen the anode layer and thermal evaporation of Aluminum cathode layer. Comparisons were made on the Surface Morphology, Electrical and Spectral characteristics of each of these layers. Higher thicknesses of organic layers deposited increased the resistance of the layer, as a result increasing the applied current and device turn-on voltage. Sheet resistance values for the annealed ITO layer were reduced to enhance electrical properties of the layer. Heating did not have any effect on the optoelectronic properties of the organic layers. Transmittance was also improved with annealing ITO to improve general efficiency of light emitted from the active layer.

Adhesion analysis was also carried out for pairwise interacting layers and its hybrid counterparts as a means of estimating interface robustness to minimize chances of failure between those with weak adhesion. Improvements in I-V characteristics were seen by incorporating TiO<sub>2</sub> nano-particles. However, this cannot also be attributed to adhesion. Although interesting results obtained from this study are only applicable on a laboratory scale, further studies can be carried out to improve existing device layer configurations and fabrication methods.

Future studies should include more I-V and J-V measurements for OLEDs/HOILEDs with a closer observation of the degradation phenomena in HOILEDs. Other forms of charge transport phenomena can be employed to better explaining the device operation. Conversely, an improved charge transport may be facilitated by high adhesion energies between these layers and this could have a positive effect on device properties. Such further work is needed

to study the degradation of charge transport on adhesion energies and contact geometry in OLEDs. Finally, better deposition techniques for depositing organic polymer layers with less roughness values on these layers.

## 5.0 References

- [1] C.W. Tang, S.A. Van Slyke, Appl. Phys. Lett. 51 (1987) 913.
- [2] M.A. Baldo, D.F. O'Brien, Y. You, A. Shoustikov, S. Sibley, M.E. Thompson, S.R. Forrest, Nature 395 (1998) 151.
- [3] Kuo C.H, Peng K.C, Kuo L.C, Yang KH, Lee J.H, Leung M.K, Hsieh K.H. High performance hole-transporting polyurethanes for light-emitting diodes applications. Chem. Mat. 2006;18:4121–4129.
- [4] R.H. Friend, R.W. Gymer, A.B. Holmes, J.H. Burroughes, R.N. Marks, C. Taliani, D.D.C. Bradley, D.A. Dos Santos, J.L. Bredas, M. Löglund, W.R. Salaneck, Nature 397 (1999) 121.
- [5] H. Aziz, Z.D. Popovic, N.-X. Hu, A.-M. Hor, G. Xu, Science 283 (1999) 1900.
- [6] Georgia Institute of Technology. Light-emitting Diodes: Understanding Factors That Influence Efficiency Of Organic-based Devices. ScienceDaily. Retrieved September, 24 2010 from <http://www.sciencedaily.com/releases/2008/07/080708105351.html>
- [7] Su Zhan, Xie Ying-ge, Li Xia, Yu Tao, Microelectronics Journal 37 (2006) 714–71
- [8] D.C. Choo, H.S. Bang, B.C. Kwack, T.W. Kim, J.H. Seo, Y.K. Kim, Thin Solid Films 516 (2008) 3610–3613
- [9] Sebastian Reineke, Frank Lindner, Gregor Schwartz, Nico Seidler, Karsten Walzer, Björn Lüssem, Karl Leo, Nature **459**, (2009) 234-238
- [10] Kao-Hua Tsai, Shu-Chia Shiu and Ching-Fuh Lin, Improving the conductivity of hole injection layer by heating PEDOT:PSS, Proc. of SPIE Vol. 7052, 70521B, (2008).
- [11] [http://en.wikipedia.org/wiki/Organic\\_LED](http://en.wikipedia.org/wiki/Organic_LED)
- [12] L.B Groenendaal, F. Jonas, D. Freitag, H. Pielartzik and J.R. Reynolds, Adv. Mater. (Weinheim, Ger.) **12**, 481 (2000); A. N. Aleshin, S.R. Williams and A.J. Heeger, Synth. Met.

**94**, 173 (1998).

[13] Barry Young, "Status of OLED Manufacturing and the search for New Applications" OLEDs 2003.

[14] Ricky Ng, "Design and Applications of OLED drivers" Solomon Systech Limited.

[15] Piromreun, Pongpun; Oh, Hwansool; Shen, Yulong; Malliaras, George G; Scott, J. Campbell; Brock, Phil J. (2000). "Role of CsF on electron injection into a conjugated polymer". Applied Physics Letters **77**: 2403.

[16] D. Ammermann, A. Böhler, W. Kowalsky, [Multilayer Organic Light Emitting Diodes for Flat Panel Displays](#), Institut für Hochfrequenztechnik, TU Braunschweig, 1995.

[17] Friend, R. H.; Gymer, R. W.; Holmes, A. B.; Burroughes, J. H.; Marks, R. N.; Taliani, C.; Bradley, D. D. C.; Santos, D. A. Dos et al. (1999). Nature **397**: 121

[18] DisplaySearch Q2 2009 Quaterly Shipment and Forecast Report, <http://www.oled-display.net/how-works-the-oled-technology>

[19] C. Adachi, M.A. Baldo, S.R. Forrest, S. Lamansky, M.E. Thompson, R.C.Wong, Appl. Phys. Lett. 78 (2001) 1622.

[20] Henk J. Bolink, Eugenio Coronado, Diego Repetto, and Michele Sessolo, Air stable hybrid organic-inorganic light emitting diodes using ZnO as the cathode, Appl. Phys. Lett. **91**, 223501 (2007)

[21] Y. Athanassoc, F. P. Rotzinger, P. Péchy, and M. Graetzel, J. Phys. Chem.B **101**, 2558 \_1997\_.

[22] Z. Zhang, Z. Deng, C. Liang, M. Zhang, and D. Xu, Displays **24**, 231\_2003\_.

[23] K. Morii, M. Ishida, T. Takashima, T. Shimoda, Q. Wang, M. K. Nazeeruddin, and M. Graetzel, Appl. Phys. Lett. **79**, 183510 \_2006\_.

- [24] S. A. Haque, S. Koops, N. Tokmoldin, J. R. Durrant, J. Huang, D. D. C. Bradley, and E. Palomares, *Adv. Mater.* \_Weinheim, Ger.\_ **19**, 683 \_2007\_.
- [25] R. Könekamp, R. C. Word, and M. Godinez, *Nano Lett.* **5**, 2005 \_2005\_
- [26] Tang, C. W.; Vanslyke, S. A. (1987). "Organic electroluminescent diodes". *Applied Physics Letters* **51**: 913
- [27] Burroughes, J. H.; Bradley, D. D. C.; Brown, A. R.; Marks, R. N.; MacKay, K.; Friend, R. H.; Burns, P. L.; Holmes, A. B. (1990). "Light-emitting diodes based on conjugated polymers". *Nature* **347**: 539
- [28] F. Huang, Y. J. Cheng, Y. Zhang, M. S. Liu, A. K.-Y. Jen, *J. Mater. Chem.*(2008) **18**, 4495.
- [29] Hong Ma, Hin-Lap Yip, Fei Huang, and Alex K.-Y. Jen, *Interface Engineering for Organic Electronics Feature article. J. of Advanced functional materials*, (2010) **20**, 1-18
- [30] J. G. C. Veinot, T. J. Marks, *Acc. Chem. Res.* 2005, **38**, 632.
- [31] A. P. Kulkarni, C. J. Tonzola, A. Babel, S. A. Jenekhe, *Chem. Mater.* **16**, (2004), 4556
- [32] G. Hughes, M. R. Bryce, *J. Mater. Chem.* 2005, **15**, 94.
- [33] J. H. Ahn, C. Wang, C. Pearson, M. R. Bryce, and M. C. Petty, *Appl. Phys. Lett.*, Vol. **85**, No. 7, (2004) 1283-1285.
- [34] Saba Zare Zardareh, Farhad Akbari Boroumand, *Int. Degradation in Organic Light Emitting Diodes, Journal of Electronics, Circuits and Systems* 3:3 (2009)
- [35] Wali O. Akande, Onobu Akogwu, Tiffany Tong, and Wole Soboyejo, Thermally induced surface instabilities in polymer light emitting diodes, *J. Appl. Phys.* **108**, 023510 (2010).
- [36] N. Bowden, S. Brittain, A. G. Evans, J. W. Hutchinson, and G. M. Whiteside *Nature*

□(London□) **393**, 146 □(1998)□.

[37] J. J. Berry, D. S. Ginley, and P. E. Burrows, Organic light emitting diodes using a Ga:ZnO anode, APPLIED PHYSICS LETTERS 92, 193304 (2008).

[38] C. C. Wu, C. I. Wu, J. C. Sturm, and A. Kahn, Appl. Phys. Lett., Vol. 70, No. 11,(1997)

[39] Huang J J, Ueng HY, Su YK, Lin SJ, Juang FS. Thickness for optimizing of organic layer and multi-layer anode on luminance efficiency in white-light top-emission organic light-emitting diodes. J Nanosci Nanotechnol. 8(10), 2008, 5176-80

[40] Katsuyuki MORII, Masayuki OMOTO, Masaya ISHIDA<sup>1</sup>, and Michael GRAETZEL, Enhanced Hole Injection in a Hybrid Organic–Inorganic Light-Emitting Diode, Japanese Journal of Applied Physics Vol. 47, No. 9, 2008, pp. 7366–7368(2008).

[41] Y. Athanassoc, F. P. Rotzinger, P. Péchy, and M. Graetzel, J. Phys. Chem.B **101**, 2558 \_1997\_.

[42] Z. Zhang, Z. Deng, C. Liang, M. Zhang, and D. Xu, Displays **24**, 231\_2003\_.

[43] K. Morii, M. Ishida, T. Takashima, T. Shimoda, Q. Wang, M. K. Nazeeruddin, and M. Graetzel, Appl. Phys. Lett. **79**, 183510 \_2006\_.

[44] S. A. Haque, S. Koops, N. Tokmoldin, J. R. Durrant, J. Huang, D. D. C. Bradley, and E. Palomares, Adv. Mater. \_Weinheim, Ger.\_ **19**, 683 \_2007\_.

[45] Henk J. Bolink, \_ Eugenio Coronado, Diego Repetto, and Michele Sessolo, Air stable hybrid organic-inorganic light emitting diodes using ZnO as the cathode, APPLIED PHYSICS LETTERS **91**, 223501 \_2007\_.

[46] T. Tong, B. Babatope, S. Admassie, J. Meng, O. Akwogu, W. Akande, and W. O. Soboyejo, Adhesion in organic electronic structures. JOURNAL OF APPLIED PHYSICS 106, 083708 □(2009)

[47] K. Morii, M. Ishida, T. Takashima, T. Shimoda, Q. Wang, Md. K. Nazeeruddin, and M.

Graetzl: [Appl. Phys. Lett. 89 \(2006\) 183510](#).

[48] 15. A. Petrella, M. Tamborra, P. D. Cozzoli, M. L. Curri, M. Striccoli, P. Cosma, G. M. Farinola, F. Babudri, F. Naso and A. Agostiano, *Thin solid films* 451-452, 64 (2004).

[49] Y. K. Kim, K. Y. Lee, O. K. Kwon, D. M. Shin, B. C. Sohn and J. H. Choi, *Synth. Met.*, 111-112, 207 (2000).

[50] J. C. Scott and P. J. Brock, *Appl. Phys. Lett.*, 71, 1145 (1997).

[51] Y. H. Kim, D. Kim, S. C. Jeoung, J. Y. Han, M. S. Jang and H. K Shim, *Chem. Mater.*, 14, 643 (2001)

[52] N. Tessler, V. Medvedev, M. Kazes, S. Kan and U. Banin, *Science*, 295, 1506 (2002)

[53] J. Cheng, S. Wang, X. Y. Li, Y. J. Yan, S. Yang, C. L. Yang, J. N.

[54] Wang and W. K. Ge, *Chem. Phys. Lett.*, 333, 375 (2001).

[55] F. Hide, B. J. Schwartz, M. A. Diaz-Garcia and A. J. Heeger, *Chem.Phys. Lett.*, 256, 424 (1996).

[56] B. O. Dabbousi, M. G. Bawendi, O. Onitsuka and M. F. Rubner, *Appl. Phys. Lett.*, 66, 1316 (1995).

[57] J. S. Salafsky, W. H. Lubberhuizen and R. E. I. Schropp, *Chem.Phys. Lett.*, 290, 297 (1998).

[58] W. U. Huynh, J. J. Dittmer and A. P. Alivisatos, *Science*, 295, 2425(2002).

[59] D. J. Milliron, A. P. Alivisatos, C. Pitois, C. Edder and J. M. J. Frechet, *Adv. Mater.*, 15, 58 (2003).

[60] L. Bakueva, S. Musikhin, M. A. Hines, T. W. F. Chang, M. Tzolov, G. D. Scholes and E. H. Sargent, *Appl. Phys. Lett.*, 82, 2895 (2003).

[61] H. Mattoussi, L. H. Radzilowski, B. O. Dabbousi, E. L. Thomas, M. G. Bawendi and M. F. Rubner, *J. Appl. Phys.*, 83, 7698 (1998).

[62] M. C. Schlamp, X. Peng and A. P. Alivisatos, *J. Appl. Phys.*, 82, 5837 (1997).

- [63] N. C. Greenham, X. Peng and A. P. Alivisatos, *Phys. Rev., B.* **54**, 17628 (1996).
- [64] Chin-Cheng Weng, Chia-Hung Chou, Kung-Hwa Wei, and Jung Y. Huang, Enhanced Electroluminescence of Poly(2-methoxy-5-(2-ethylhexyloxy)-1,4-phenylene vinylene) Films in the Presence of TiO<sub>2</sub> Nanocrystals, *Journal of Polymer Research* vol **13**, (2006) 229–235
- [65] H. Kim, C. M. Gilmore, A. Piqué, J. S. Horwitz, H. Mattoussi, H. Murata, Z. H. Kafafi, and D. B. Chrisey, Electrical, optical, and structural properties of indium–tin–oxide thin films for organic light-emitting devices. *J. Appl. Phys.* **86**, 6451 (1999)
- [66] C. C. Wu, C. I. Wu, J. C. Sturm, and A. Kahn, Surface modification of indium tin oxide by plasma treatment: An effective method to improve the efficiency, brightness, and reliability of organic light emitting devices. *Appl. Phys. Letter* **70**, 1348 (1997)
- [67] Furong Zhu, Keran Zhang, Bee Ling Low, Shuang Fang Lim, Soo Jin Chua, Morphological and electrical properties of indium tin oxide films prepared at a low processing temperature for flexible organic light-emitting devices. *Materials Science and Engineering* **B85** (2001) 114–117
- [68] Takayuki Uchida, Makoto Wakana, Toshifumi Satoh, Effect of annealing on plastic substrate with ITO used in flexible OLEDs, Center for Hyper Media Research, Tokyo Polytechnic University.
- [69] <http://www.ucsf.edu/tchriste/courses/PHYS549lectures/evap.html> *J. Phys. Condens. Matter.* 2002; **14**: 9825-9876
- [70] I Sridhar, Z W Zheng and K L Johnson, A detailed analysis of adhesion mechanics between a compliant elastic coating and a spherical probe, *J. Phys. D: Appl. Phys.* **37** 2886 (2004)
- [71] J.A. Greenwood, "Adhesion of Elastic Spheres", *Proc. R. Soc. Lond. A* (1997) **453**, 1277-1297
- [72] K. L. Johnson and K. Kendall and A. D. Roberts, Surface energy and the contact of

elastic solids, Proc. R. Soc. London A 324 (1971) 301-313; Johnson, KL and Greenwood, JA, 1997, An adhesion map for the contact of elastic spheres, Journal of Colloid and Interface Science, 192(2), pp. 326-333.

[73] Derjaguin, BV and Muller, VM and Toporov, Y.P., 1975, Effect of contact deformations on the adhesion of particles, Journal of Colloid and Interface Science, 53(2), pp. 314-326.

[74] Muller, VM and Derjaguin, BV and Toporov, Y.P., 1983, On two methods of calculation of the force of sticking of an elastic sphere to a rigid plane, Colloids and Surfaces, 7(3), pp. 251-259.

[75] [http://en.wikipedia.org/wiki/Contact\\_mechanics#cite\\_note-Tabor1-27](http://en.wikipedia.org/wiki/Contact_mechanics#cite_note-Tabor1-27)

[76] Tabor, D., 1977, Surface forces and surface interactions, Journal of Colloid and Interface Science, 58(1), pp. 2-13.

[77] D. Maugis, Adhesion of spheres: The JKR-DMT transition using a Dugdale model, J. Colloid Interface Sci. 150 (1992) 243—269

[78] <http://en.wikipedia.org/wiki/File:MaugisDugdale.svg>

[79] Carpick, R.W. and Ogletree, D.F. and Salmeron, M., 1999, A general equation for fitting contact area and friction vs load measurements, Journal of colloid and interface science, 211(2), pp. 395-400

[80] O. Piétrement and M. Troyon, General Equations Describing Elastic Indentation Depth and Normal Contact Stiffness versus Load. Journal of Colloid and Interface Science 226, 166–171 (2000).

[81] McGraw-Hill Concise Encyclopedia of Physics. © 2002 by The McGraw-Hill Companies, Inc.

- [82] The Great Soviet Encyclopedia, 3rd Edition (1970-1979). © 2010 The Gale Group, Inc
- [83] Millikan, R. A., and C. C. Lauritsen. *Phys. Rev.*, 1929, vol. 33, no. 4, p. 598
- [84] D. Braun, Ph.D. Thesis, University of California, Santa Barbara, 1991.
- [85] K. V. Wolf, Z. Zong, J. Meng, A. Orana, N. Rahbar, K. M. Balss, G. Papandreou, C. A. Maryanoff, and W. O. Soboyejo, *J. Biomed. Mater. Res. Part A* 87A, 272 □2008□.
- [86] Fowler, R. H., and L. Nordheim. *Proc. Roy. Soc., series A*, 1928, **vol. 119**, no. 781, p. 173.